

Asteroid Trails in Hubble Space Telescope¹

WFPC2 Images : First Results

Robin W. Evans^{2,3}, Karl R. Stapelfeldt², Daniel P. Peters², John T. Trauger², Deborah L. Padgett⁴, Gilda E. Ballester⁵, Christopher J. Burrows⁶, John T. Clarke⁵, David Crisp⁷, Jay S. Gallagher⁸, Richard E. Griffiths⁹, Carl Grillmair², Jeff J. Hester¹⁰, John G. Hoessel⁸, Jon Holtzman¹¹, John Krist⁶, Matthew McMaster⁶, Vikki Meadows², Jeremy R. Mould¹², Eric Ostrander⁹, Raghvendra Sahai², Paul A. Scowen¹¹, Alan M. Watson¹¹ and Jim Westphal¹³

¹ Based on observations with the NASA/ESA Hubble Space Telescope

² Mail Stop 183-900, Jet Propulsion Laboratory, 4800 Oak Grove Drive, Pasadena, CA 91109

³ e-mail address rwe@wfpc2-mail.jpl.nasa.gov

⁴ Infrared Processing and Analysis Center, Mail Stop 100-22, California Institute of Technology, Pasadena, CA 91125

⁵ University of Michigan, Dept. of Atmospheric, Oceanic and Space Sciences, 2455 Hayward, Ann Arbor, MI 48109-2103

⁶ Space Telescope Science Institute, 3700 San Martin Drive, Baltimore, MD 21218

⁷ Mail Stop 169-237, Jet Propulsion Laboratory, 4800 Oak Grove Drive Pasadena, CA 91109

⁸ University of Wisconsin, Madison, Dept. of Astronomy 475 N. Charter St., Madison, WI 53706

⁹ Dept. of Physics, Wean Hall 8311, Carnegie-Mellon University, 5000 Forbes Ave., Pittsburgh, PA 15213-3890

¹⁰ Arizona State University, Dept. of Physics and Astronomy, Tyler Mall, Tempe, AZ 85287

¹¹ Dept. of Astronomy, New Mexico St. University, Box 30001 Dept. 4500, Las Cruces, NM 88003-8001

¹² Mt. Stromlo and Siding Spring Observatories, Private Bag, Weston Creek P.O., A.C.T. 2611, Australia

¹³ California Institute of Technology, Mail Stop 170-25, Pasadena, CA 91125

Keywords: Asteroids; Hubble Space Telescope

Suggested Running Head: Space Telescope Asteroid Trails

Correspondence should be sent to Dr. Robin Evans

Mail Stop 183-900, Jet Propulsion Laboratory, 4800 Oak Grove Drive, Pasadena, CA 91109

e-mail address rwe@wfpc2-mail.jpl.nasa.gov

Voice: (818) 354-1027

FAX: (818) 393-9088

ABSTRACT

Careful examination of 28,460 selected Wide Field and Planetary Camera 2 (WFPC2) long exposures from 1994, 1995 and early 1996 has revealed trails of 96 distinct moving objects. They have been reported to the International Astronomical Union's (IAU) Minor Planet Center for their asteroid database and a few have been identified with known asteroids and used to update their orbits. Most of the objects are new, as they are too faint to show up on ground-based surveys.

The trails often show a characteristic curvature due to the parallax induced by HST's orbital motion during the exposures. *Using ephemerides for HST, the distance to each object can be directly determined from the parallax contribution to the trail shapes.* Based on these distances, constraints on the orbits, and photometry of the trails ($16 < V < 24$), most of the moving objects appear to be small, main-belt asteroids a few km in diameter. A few are known objects; three are potential Mars crossers. Modern wide-field CCD surveys detect asteroids nearly as faint as these ($V < 21$), but the corresponding absolute magnitudes are uncertain unless their orbits have been established.

The detected objects span the absolute magnitude range $13.6 < H < 19.3$ (H is the symbol for absolute magnitude, not H-band). Statistics of the detections imply a reservoir of $(3.1 \pm 0.6) \times 10^5$ such asteroids within 25° of the ecliptic. We find that the slope of the cumulative distribution of absolute magnitudes follows a power law $N \propto H^{0.2}$ to $N \propto H^{0.3}$ over this absolute magnitude range in the three distances ranges defined by the Palomar-Leiden Survey. These are significantly shallower slopes than those inferred by the Palomar-Leiden survey or extrapolated from population studies of larger asteroids.

I. Introduction

Asteroid research has always been plagued by limiting magnitude. The limiting magnitude for detectability of an asteroid of a given size is a function of both its distance from the Earth and the albedo (or type) of the asteroid. Modern ground-based, wide-field asteroid surveys are limited to about magnitude 20 (Mikami and Ishida 1987, Whipple *et al.* 1995) which limits the size of observable asteroids to approximately 1–10 meters for Earth crossers, 1 km for Mars crossers and inner main belt asteroids, 5 km for outer main belt asteroids, and 12 km for Trojan asteroids (assuming C type: Hughes and Harris 1994, Xu *et al.* 1995). A low albedo C-type asteroid needs to be twice the diameter of an S-type (high albedo) to be observable at the same distance. The Spacewatch program (Waldrop 1982, Gehrels, *et al.* 1992) at Kitt Peak has a detector with a field of view 4 times that of WFPC2 and reaches $V \approx 21$. This is not a wide field survey program but because it is dedicated to scanning for asteroids and is automatic, it has an impressive record of asteroid observations.

The population statistics for small, main-belt asteroids, as well as the Trojans, are important for models of solar system history. A few of the largest asteroids are thought to be original accretion objects that survived without later catastrophic breakup; the rest are remnants of the breakup period which is probably not over (Yuasa 1983). The impact record on Gaspra implies that it may be only a few hundred million years old (Chapman *et al.* 1994). Further, it is believed that the Ida–Dactyl system was produced in a breakup of a larger object but that Dactyl’s orbit is probably not stable over solar system age time scales. However there are disagreements on these time scales (e.g. Farinella *et al.* 1989).

Above a diameter of 130 km the asteroid population is reported to be completely accounted for and follows a power law for log-cumulative-number vs. log-diameter (Hughes 1982, Donnison and Sugden 1984, Hughes and Harris 1994). Below the 130 km size limit, the population power law slope is observed to be less steep than seen for larger asteroids (Cellino *et al.* 1991; Ishida *et al.* 1984). This change in slope could be explained by the incompleteness of the sample at smaller sizes in these surveys, or by a real population change such as the transition between the initial size distribution of objects at their time

of formation versus a size distribution dominated by subsequent collisional evolution.

There is also a question of whether the Trojans are a more significant group of asteroids than presently indicated (Hughes and Harris 1994), rivaling the population of main belt asteroids. This is important for studies of Jupiter's role in asteroidal interactions, the question of whether the mass in the main asteroid belt was much higher in the past, and the relative importance of asteroid versus comet impacts in the inner solar system's past. Finally, knowledge of the population of small asteroids is important for estimating the past and future frequency of large impacts on the Earth.

The Hubble Space Telescope (HST) is not designed for asteroid surveys. The time and number of exposures required to photograph a significant fraction of the sky near the ecliptic would be prohibitive. Luckily the HST is prolific in the number of exposures made in the course of its astronomical duties and moving objects are unavoidably captured in many images. Most such objects would be expected to be small, main-belt asteroids since their large number gives a greater probability of being accidentally observed in HST's narrow field of view. Although the telescopic magnitude limit ($V \approx 28$ in a single orbit) cannot be reached in a trailed asteroid, asteroids the size of Dactyl ($r \approx 1$ km: $19 < V < 22$ (S-type) and $21 < V < 24$ (C-type)) and smaller should be detectable throughout the main belt. HST asteroid trails therefore provide a new lower limit on the size of objects that can be detected.

II. Observations

An initial asteroid trail was discovered in an image from the GTO Parallel Survey. A review of 1680 available Survey images produced 12 more objects and was encouraging enough to motivate a comprehensive search of WFPC2 images. We restricted the search to images made in broad-band (but not ultraviolet) filters, and with exposure times of 300 seconds or longer. All WFPC2 images satisfying these criteria, and which were publically available one year after their epoch of observation, were retrieved from the Space Telescope Science Institute (STScI) Archive. No ecliptic latitude discrimination was employed. This data set was augmented by Medium Deep Survey (MDS) images and the Hubble Deep

Field (HDF). The total database comprised 7115 pointings, each with 3 Wide Field and 1 Planetary Camera image. This corresponds to 28,460 CCD images selected from all WFPC2 images made through early 1996. Figure 1 shows the sky coverage of this data set.

Asteroid trails are most easily discovered by comparison of two or more consecutive raw frames at the same pointing. The technique used is to display two such exposures simultaneously on a computer workstation by placing each image in a separate color video plane. In this rendering, fixed objects in the field appear in grayscale, or in slight color if different color filters or unequal exposure times were used. Any features which are different between the two images stand out strongly in color. By far the most common difference between the images is the multitude of cosmic ray tracks, which are a ubiquitous noise source in CCD images made from low Earth orbit. A moving object trail is easily recognizable by eye amidst this background noise by the continuity of its brightness and motion across both images. It also appears slightly broadened by the telescope point spread function, a feature not shared by cosmic rays. Faint cosmic ray trails are rare, so moving object trails which are too dim to show the telescope point spread function can also be recognized. Trails that appear on only a single frame are also readily identified. It was difficult to conceive of an automated computer recognition algorithm which would reliably identify real trails near the noise level, and all trails reported in this paper were discovered by eye. The observer improves with experience: the first data set that produced 12 trails was later re-examined and 3 additional very dim trails were discovered. Completeness is probably lacking in the case of very dim short trails; these mimic the myriad of short cosmic ray tracks and are lost in the noise. Completeness may also be lacking in complex fields where the HST primary science target shows detailed image structure.

It is immediately obvious that asteroid trails in HST images are very different from those seen at ground-based observatories. *HST asteroid trails are usually curved.* This curvature is not due to motion of the asteroid itself, but rather to the parallax caused by HST's orbital motion around the Earth during the exposures. During a typical 15 minute exposure, the position of HST will shift by about 1 Earth radius. For main belt objects near opposition (distance from Earth, $\Delta \approx 2$ AU), the magnitude of the parallax is on the order

of $\arctan(R_E/2 \text{ AU}) \approx 4''$. Stellar aberration is completely compensated by HST's pointing control system and does not contribute to the trail shapes. This distinctive curvature also helps to distinguish moving objects from cosmic ray tracks, which are usually straight.

Figures 2–4 show representative asteroid trails as seen in multiple consecutive exposures which have been rendered in red and blue color planes. Figure 2 shows an asteroid seen only in one exposure, and which had exited the field of view before the second exposure started. Note that the trail's definition is confused at locations where it intersects cosmic rays and background stars. Figure 3 shows an asteroid captured in four consecutive HST exposures. The asteroid enters the field from the lower right edge in the first exposure, shown as an incomplete red trail. The second exposure shows a complete trail in blue. HST subsequently moves behind the Earth as seen from the asteroid, then in the next orbit two complete trails are seen as the second red/blue pair. Note that an Earth orbiting satellite moves completely across the field in the second exposure causing photometric problems where it crosses near the asteroid trail. Also note the confusing effects of the many cosmic rays, and of background galaxies. Figure 4 shows a 200 x 200 pixel subimage showing an asteroid trail pair near the image noise level. This magnitude 23 object is near the limit of what can be reliably detected and photometered. Dimmer asteroids can produce brighter trails if they have smaller rates of apparent motion.

III. Results

From the total of 28,460 WFPC2 images searched, we identified 230 images with moving object trails. In most cases the trails are seen in consecutive frames made during the same HST orbit, and in a few cases they are also seen in frames from the following orbit. Only 96 distinct objects have been observed. Four of these asteroids were found during routine data quality checking by the WFPC2 group at STScI and were analyzed with the appropriate Principal Investigator's permission. Very few trails were found in Planetary Camera images, where the smaller field of view and lower photometric sensitivity strongly select against random detections of very faint objects. Not included in the 230 images with trails are many images where long, straight trails were observed to pass completely across

the WFPC2 field of view. We identify these as objects very near the Earth, most likely artificial satellites (or “space junk”) which cross our narrow 140'' field of view so rapidly that no curvature or endpoints can be seen. However, in two cases (objects u280fr02t2 and u2c4090ct2–u2c4090ct3) trails of very nearby objects show apparent endpoints due to their intrinsic brightness variations on short timescales.

Table 1 lists the images in which asteroid trails were found. The HST Archive designation of the image, the filter used, and the apparent magnitude of the object are given. Usually one of the two “V” filters, F555W and F606W, was used; we ignore the distinction between them. In some cases, an object seen in multiple exposures will also have been observed in more than one photometric filter. This allows color information to be determined in the WFPC2 photometric system. Usually the available color is (V–I), which can be diagnostic of the various mineralogic absorption features (Gaffey 1989) seen in the I band. For the dimmest objects these colors are not reliable because absolute photometry errors exceed the differences in magnitudes.

To check the possibility that some of the HST asteroid trails correspond to known objects, we compared the positions to epoch of observation positions for $\approx 31,000$ objects given in the Lowell Observatory asteroid orbital elements database (astorb.dat; *Bowell et al.* 1994). We adapted subroutines from the Jet Propulsion Laboratory’s NAIF/Spice routines (Acton 1996) to propagate the orbits. This method is sound but is subject to significant errors if the orbital elements are out of date. This method and later identifications by the MPC combined to yield seven HST objects that appear to correspond with previously known objects. They are discussed in section IV c.

The right ascension and declination are calculated in the images using the header information for the telescope pointing and orientation. Some headers provide pointing information for the PC1 camera only; for these images we determined fixed offsets from this to the WF2, WF3, and WF4 cameras by measuring the position of fiducial “K–Spots” in WFPC2 calibration images. HST absolute pointing is quoted to be good to 3 pixels (0.3'') in the WFPC2 Instrument Handbook. In some cases with multiple exposures of the same field, the headers were observed to disagree by as much as 10''. These offsets

were measured directly from object positions in the images, and then verified or corrected. The telescope pointing history (“jitter”) information for the exposures can be helpful in deciding which absolute pointing is correct. Usually these cases occur when the standard header is not updated to reflect subsequent target offsets and so only the first image has the correct pointing.

Each asteroid track was astrometrically defined by calculating the position on the sky of each pixel along the trail. Sub-pixel positions were used for the brighter trails by weighting photometry (centroiding) perpendicular to the track. Timing information is only available for the track endpoints; the intermediate pixels define a shape only. The endpoints of each trail correspond to the beginning and end of each exposure, for which the Universal Times (UT) are given by the the image header cards EXPSTART and EXPEND. Light curves are apparent in some of the tracks but relative HST/Earth–asteroid motion is the dominant contributor to these variations. It is expected that the light from the asteroid itself would vary little in the 20 minutes of a long exposure. Slight variations due to the asteroid may have been observed in a few cases where HST tracking of the object was over multiple orbits (hours).

Photometry of the trails is performed by de-biasing and flat-fielding the image, then subtracting a local background adjacent to the trail (e.g. the sky, M87, etc). Counts are then summed avoiding any pixels affected by cosmic ray hits but using a count of hit and non-hit pixels as a scaling factor to correct for the missing pixel values. The asteroid’s magnitude in the particular filter is then measured following procedures described in the WFPC2 Instrument Handbook. Photometry errors are a function of brightness of the asteroid, length of the trail, image background level, astronomical objects in the field of view which contaminate the trail, and cosmic ray hits. We would like here to redefine “the vermin of the sky” as those pesky little distant galaxies that keep contaminating HST asteroid trails.

IV. Analysis of the Individual Trails

a). Distance and Angular Motion Determination

The parallax induced by the orbital motion of HST provides a unique opportunity to determine the distance to each asteroid from a single resolved trail. To do this we must compare the observed trail to predicted trails appropriate to the specific circumstances of an HST observation, and seek a best-fit solution by varying the geocentric distance. We consider a trail to consist of two distinct components. First is the time-varying parallax induced by *both* the orbital motions of HST about the Earth and of the Earth about the Sun. We used Keplerian orbital elements for HST supplied in the standard header for each image; typically these elements are current to within a few hours of the time of the exposure. Our program *hsteroid* calculates the Cartesian equatorial position of HST versus time from these elements, and calculates the Earth's motion using the Jet Propulsion Laboratory's NAIF/Spice routines (Acton 1996). Combining this with the known HST-Earth-Asteroid geometry, *hsteroid* predicts a parallax track $\vec{P}(\Delta, t)$ valid during the image exposure interval for an object at a specific geocentric distance Δ and t is the elapsed time since the shutter opened.

The second independent component of the trails is the *heliocentric* orbital motion of the object on the plane of the sky as seen from Earth. We assume this will appear as uniform linear motion during the short duration of an exposure sequence (3 hours or less). Thus in principle there are two additional parameters needed to describe the trails, which we term the *geocentric intrinsic rates of motion* in right ascension and declination ($\dot{\alpha}, \dot{\delta}$ respectively). At any time during the exposure, the position of the moving object is a linear combination of these rates and those induced by parallax:

$$\alpha - \alpha_0 = P_\alpha(\Delta, t) + \dot{\alpha} \cdot t$$

$$\delta - \delta_0 = P_\delta(\Delta, t) + \dot{\delta} \cdot t$$

where (α_0, δ_0) is the initial position of the object, P_α and P_δ are the two components of the vector \vec{P} . The observations provide an important boundary condition, which is that the combined displacement produced by the parallax and geocentric intrinsic rates over the exposure time must equal the observed distance between the trail endpoints. This allows

$\dot{\alpha}, \dot{\delta}$ to be calculated directly from known quantities; for each trial value of Δ , there exist unique values for $\dot{\alpha}, \dot{\delta}$ which are consistent with the observations.

Our program *hsteroid* calculates the χ^2 difference between model and observed trails as a function of the single unknown parameter Δ . Multiple trails from consecutive images are used in a simultaneous solution when available as long as both endpoints can be seen. For 31 objects only a single trail is available; in these cases we adopted the direction of motion as being that which produced the best χ^2 fit to the trail. This agrees with most cases where the angle from opposition indicates an obvious induced prograde/retrograde motion. In a few cases, we were able to improve the solution for a single complete trail by including the visible endpoint from a partial trail seen in an adjacent exposure.

Figure 5 shows various samples for the functional fits for the trail shown in Figure 2 (u2805m01t4). The reduced χ^2 minimum shown in the top panel is for an Earth–asteroid separation of .93 AU. The resulting model trail for four trial distances is plotted with the data in the bottom panel. The three lines labeled are for solutions that do not minimize χ^2 and are shown to illustrate the trail fitting procedure. All solutions are forced to intersect the trail endpoints, which are unique in that the time when the object was at these positions is known. Once the endpoints are fixed the curvature and shape of the model track is dependent only on the HST/Earth–asteroid geometry (known) and the distance (unknown). The solution for $\Delta = .93$ AU is seen overlying the datapoints. This magnitude 18.7 asteroid is at heliocentric distance of $1.68 \pm .03$ AU with an angle from opposition (opposition = 0°) of 58° . It is probably a Mars crosser.

Fits to the trail shapes are good in the majority of cases, and these results are shown in Table 2. We adopted a characteristic measurement error of $\pm 0.05''$ (0.5 WF pixel) for the relative astrometry along the asteroid trails. The reduced χ^2 differences between the best–fit model predictions and the observed data points then range from 0.2–4.4, with a median value of 0.7. These equate to a median angular residual of $0.04''$ per data point. Uncertainties quoted for the geocentric and heliocentric distances in Table 2 correspond to distances where χ^2 has increased from the optimal solution by exactly a value of 1. The best–determined distances are found for trails which show the greatest amount of

curvature.

In forty-two cases, trail fitting either could not be performed or yielded a distance solution with large error bars. These objects are listed in Table 3. Single incomplete trails cannot be fit since the object's position is unmeasured at either the beginning or end of the exposure; there were six such cases. Another five trails were imaged while HST was tracking another moving target. These were not fit because the effect of the tracking rates must be removed from the observed trails, and our software does not yet treat this scenario. For the final thirty-one objects, poor distance solutions are obtained because the observed trails are nearly straight. In these cases HST's orbit plane lies nearly parallel to the net linear motion of the object (its own heliocentric motion and Earth parallax), precluding a clean separation of HST's parallax contribution to the trail shape.

Besides straight trails, difficulties can occur when fitting objects that have near stationary motion with respect to HST/Earth. The object in images u280fv01t4–u280fv02t4 goes stationary in between exposures and the object in u2ov6f01t4–u2ov6f04t4 is seen to move almost purely North–South in three images and East–West in the last. These cases cause problems because there is no one-to-one correspondence between (α, δ) within the trails. Good fits can be achieved if trail segments producing these redundancies are omitted.

Figures 6 and 7 show how the degree of complexity in the trail structure controls how well the distance can be solved for. Figure 6 is the fit to asteroid u2b40405t3 which is seen in three consecutive HST orbits and moves through three of the WFPC2 cameras. The extent and curvature of the trails lead to an excellent fit. This magnitude 21.8 asteroid is at heliocentric distance of 2.37 ± 0.01 AU with an angle from opposition of 34° . Figure 7 is a fit to asteroid u26g0e02t4. The fitted distance has large error bars due to the lack of sufficient trails curvature, as discussed above. This magnitude 22.3 asteroid is at heliocentric distance of 2.6 ± 0.3 AU with an angle from opposition of 31° .

Figure 8 shows a fit to asteroid u26g0601t4 which is an interesting case of a prograde–retrograde loop. Combined HST and Earth motion leads to the apparent retrograde motion of the asteroid in the imaged trails. Between the exposures, HST is moving in a direction

opposite to Earth's motion and the difference is slow enough that the asteroid moves prograde. This magnitude 18.9 asteroid is at heliocentric distance of $2.63 \pm .05$ AU with an angle from opposition of 54° .

b). Orbits

Classically, multiple ground based observations taken over a long period of time are required to derive useful orbital information for an asteroid. The WFPC2 camera has sufficient resolution so that one exposure can be considered two classical observations, if the direction of motion along the trail can be determined. Two exposures will give the direction of travel. For each exposure the available information is a starting time, start location (right ascension and declination), and an ending time and ending location. Unfortunately classical methods (Gauss, Laplace, etc.) fail when used with observations taken this close in time (≈ 1000 seconds). The problem is an unmeasured velocity component in the direction of the observer, or a lack of acceleration history of the asteroid. We therefore measure only 5 of the 6 necessary parameters for a complete orbital solution. However, some constraints can be placed on the asteroid orbital elements by making use of the geocentric distance determined by parallax fitting of the trail.

The first step is to calculate the heliocentric position of each asteroid in three dimensions using its geocentric coordinates (Δ, α, δ) and the known position of the Earth at the time of the observations. The resulting heliocentric distances r are given in Table 2 and the distribution of those with good fits is shown in Figure 9. The distribution of r shows that nearly all the objects with well-determined distances lie within the main asteroid belt ($2.0 < r < 3.7$ AU) near the ecliptic plane. In addition to the location of the asteroid, the distance determination allows two components of the asteroid space velocity to be directly calculated from the observed geocentric intrinsic angular velocities. The third component, the geocentric radial velocity, is unknown but can be bounded by the assumption that the objects are moving at less than solar system escape velocity at their heliocentric distance. For the objects with well-determined distances, the semi-major axis, eccentricity, and inclination were calculated over the full range of possible geocentric radial velocities. This results in a family of orbit solutions consistent with the observations; an example case is

shown in Figure 10. Table 4 lists the ecliptic latitude, right ascension rate, declination rate and orbit constraints for the asteroid trails with good distance solutions. The elements obtained show again that the trailed objects in the WFPC2 images are consistent with main belt asteroids.

Complete orbit solutions for the objects studied here will only come if they are recovered by future observations. Unfortunately, most of these asteroid trails were discovered in archival data as much as a year after the observations were made. Thus the available orbit information derived from the trails is insufficient to give much chance that targeted recovery observations would succeed; the time delay between discovery and first follow-up would be too long. The Minor Planet Center (MPC) has stated that they will archive these observations as an unpublished database for potential future identifications.

c). Noteworthy Objects

The brightest trail in this database appeared in images u2om1201t4–u2om1204t4. This object was immediately noticed during a routine data quality review at Space Telescope Science Institute, and was reported to us only a few weeks after observation (and after obtaining the Principal Investigator's permission). Analysis of the trails was performed and reported to the MPC, where it was identified with contemporaneous reports of 1995 SS₃ made by Japanese amateurs K. Endate and K. Watanabe. It was later identified with the object 1222 T–1 seen in 14 separate observations since 1971. Full orbit solutions for this object have been published in Minor Planet Circulars 19265, 26185, and 26423; the latter includes the HST observations. The known ephemeris for this object provides an ideal test of the HST asteroid trail analysis. At the time of the HST observations, the ephemeris shows that the object was at 0.98 AU from the Earth and 1.93 AU from the Sun. The parallax fitting results given in Table 2, 0.96 ± 0.02 AU and 1.91 ± 0.02 AU, are in excellent agreement with these values. Furthermore, the actual orbital elements of 1222 T–1 ($a = 2.43$, $e = 0.233$, $i = 11.29$; MPC 26423) lie within the bounds derived from the trail analysis ($a > 2.32$, $e > .21$, and $7.5 < i < 19.5$). This comparison therefore validates the methods used herein to derive parallax distances and orbit constraints.

Another previously discovered object, 1992 UY₃, can be identified with the trail u26g0601t4. The HST position is 75'' from that predicted using the existing elements ($a=2.26$ AU, $e=0.18$, and $i=05.2^\circ$, from the Lowell Observatory 19970601 astorb.dat database). Our calculation of the asteroid ephemeris predicts an Earth distance of 1.92 AU. Trail fitting finds an Earth distance of 1.94 ± 0.06 AU, and constrains the orbit to $a > 2.01$, $e > .02$ and $5.3^\circ < i < 6.4^\circ$. Again, the agreement seen is quite satisfactory. Object u27z5601t3 lies 15' from the predicted location of numbered object 5825, and the MPC identified the two as the same object. The bright trail u2e61p01t4 lies only 85'' from the predicted position of 1973 RF. The MPC has made the same identification; however, this trail was too straight to yield a useful distance solution. Two other possible identifications noted by the MPC, 1990 QN₉ with u2805v01t2 and 1992 EB₁₃ with u27yg701t3, also do not provide tests of our method because of an ill-defined endpoint and a straight trail, respectively.

Object u26g0d01t4 is an interesting case of a single trail where the direction of motion is ambiguous. This object crosses the outer corner of the WF4 detector, and thus its absence in prior and subsequent images of the field provides no clue as to direction of travel. The best-fit solution ($\chi^2 = 0.51$) corresponds to retrograde heliocentric motion, $r = 2.38$ AU, and an object highly unbound to the solar system. Assuming the opposite direction of motion gives a fit which is not as good ($\chi^2 = 2.03$), but corresponds to a bound orbit and more realistic prograde motion at $r = 1.74 \pm 0.33$ AU. Since both solutions are satisfactory, we adopt the more likely prograde solution in Tables 2 and 4. The MPC has identified this object as 2278 Gotz, for which our propagation of the elements (Lowell Observatory 19970601 astorb.dat) predicts a position only 257'' from that seen by HST. However, the heliocentric distance of 2278 at the epoch of observation ($r = 2.59$ AU) is significantly different from the value derived from the parallax fitting. Thus the identification of u26g0d01t4 with 2278 may only be coincidental.

Three asteroids have heliocentric distances and orbit constraints which suggest they are Mars-crossers. Object u2805m01t4 lies at a heliocentric distance of only 1.68 AU and ecliptic latitude of -23° . The orbit constraints dictate that this is a Mars-crossing object, and possibly an Earth-crosser as well. It could be an Apollo or Amor object, although a

cometary orbit cannot be ruled out. The object in u33l3801m3 has been identified as 1997 GQ₂₅, an object observed shortly before by Spacewatch and found to have a perihelion distance of 1.62 AU. The other object that could be a Mars crosser is u2ov5601t2 with a minimum semi-major axis of 1.25 AU. This asteroid was a small distance outside Mars' orbit at the time of observation.

In several cases, multiple asteroids cross the field of view during observations of a single field. Two asteroids appear in image u2ar0c03t3 with a separation of 100'', but do not share a common apparent motion. The object seen in image u26g0e01t3 is suspiciously similar in brightness and direction of motion to another object in the following images u26g0e02t4–u26g0e03t4, but is offset by 2'. A simultaneous solution of all three trails is not possible, and the u26g0e01t3 trail is too straight to give a useful solution by itself. A bright asteroid in u2sw0501t1 that has an endpoint in a saturated star is accompanied by a much fainter asteroid that has the same parallax motion. Other rich fields were found in the programs doing deep imaging near the ecliptic. A program to detect Kuiper belt objects (images u2hn*) produced five asteroids, and exposures of Comet Shoemaker–Levy 9 yielded another five.

d). Photometry and Size Estimates

Assuming an S-type asteroid albedo, we have derived absolute magnitudes, and sizes for asteroids with good distance fits. These parameters are listed in Table 2. It should be noted that the photometry is at best 2% accurate, and is worse when cosmic ray tracks intersect the asteroid trail. Absolute magnitudes were derived using Earth and Sun distances given in Table 2 and a phase angle (derived from the measured angle from opposition and these two distances); sizes were derived assuming an albedo of 0.15 in all filters and using the empirical expression (equation 8) given in *Bowell and Lumme 1979*. The derived sizes are radii of an equivalent reflecting sphere and have large errors due to the unknown albedo.

The asteroids range in absolute magnitude from 13.6 to 19.3. Object u2hn0301t4 is the smallest at $R = 0.24$ km. Object u2805v01t2 is the largest $R = 3.3$ km. Errors are not

listed for the radii but they relate directly to the errors in the distances and magnitudes of the objects and are dominated by the assumption of an albedo of 0.15. A change in the albedo of ± 0.1 would change the radius by $\pm 50\%$.

e). Detectability of Small Comets

Frank *et al.* 1986 has claimed that the Earth is subject to a steady rain of stealthy mini-comets with an albedo ≈ 0.02 , diameter of 10 meters, relative velocity of 10 km sec^{-1} , and impact rate with Earth of 5–30 impacts per minute. Given the above assumptions, such objects will have an absolute opposition magnitude $H \approx 30$. At non-zero phase angles such objects will appear fainter. HST's Sun avoidance constraint restricts the range of possible phase angles to be less than 130° . We assume the phase effect of non-opposition geometry will reduce the apparent brightness of such objects by about 2 magnitudes. We now briefly consider how many $H \approx 32$ objects near the Earth should be detected in the present HST data set.

To be detected by HST, the brightness and angular motion of the mini-comets must combine to exceed our estimated photometric detection limit of 2 DN (14 photoelectrons) per $0.1''$ pixel. HST's orbital motion would combine with that of the targets to give a relative velocity on the order of 15 km sec^{-1} . Assuming that this would be manifest entirely as transverse motion, the dwell time (in seconds) during which a moving object traverses a single WF pixel will then be $t = \Delta(\text{km})/3 \times 10^7$. Using this as an effective "exposure time" per pixel, we derive from the known WFPC2 photometric performance the maximum distance at which the signal from an $H=32$ object will exceed our detection threshold. This is $\Delta_{\text{max}} = 40,000$ to $60,000 \text{ km}$ for the most commonly used filters in our dataset. A 10 m object will be spatially unresolved by the WF cameras at distances beyond 20,000 km, and will cross a WF camera field of view in about 1 second at 40,000 km or 1.6 seconds at 60,000 km. These objects will cross the complete WFPC2 field of view in 2 to 3 seconds, and thus a typical 1000 sec exposure will contain 300–500 statistically independent samples of the sky for such objects.

To maintain a steady infall rate $r = 5 \text{ objects min}^{-1}$, the volume density of mini-

comets will be given by $N = r/\pi R_E^2 v$. This corresponds to one object per $1.5 \times 10^{10} \text{ km}^3$. This minimal volume density suggests that 20,000 to 60,000 mini-comets would be close enough to be detected by HST at any given instant for the above range in Δ_{max} . However, WFPC2's narrow field of view corresponds to a solid angle of only 4.2×10^{-7} steradians. To the limiting outer radii for detection of mini-comets, the volume searched is just 9×10^6 to $3 \times 10^7 \text{ km}^3$. Depending on the choice of Δ_{max} , there are 300–500 independent samples of this volume during a typical 1000 sec exposure. The expected detection rate of mini-comets would be 0.3–0.6 per exposure assuming an infall rate of $r = 5 \text{ objects min}^{-1}$. In our entire dataset of 7115 exposures, 2000–4000 such objects should have been seen. We see 94 asteroid trails, two unknowns and 233 satellite trail candidates in this data set, for a grand total of 329 objects. Unresolved satellite trails are probably indistinguishable from the trails of mini-comets. If all 210 unresolved satellite trail candidates were actually mini-comets, then an upper limit to the mini-comet detection rate is obtained which is an order of magnitude smaller than that predicted by Frank *et al.* 1986a and b. However, it is likely that most (if not all) of the unknown objects are satellite trails, and thus the number of mini-comets in our data set would only be a small fraction of the 210 unresolved satellite trail candidates. Thus the archival HST data appears to seriously limit the population of mini-comets near the Earth proposed by Frank *et al.* (1986).

V. Detection Statistics and their Implication for the Population

a). Main Belt

In this survey asteroids are detected in 84 out of 1671 exposures within 10° of the ecliptic, 8 out of 1216 exposures taken between 10° and 25° of the ecliptic, and 4 (1 probable space junk) out of 4228 exposures for images taken at ecliptic latitudes greater than 25° . The combined field of view of the four WFPC2 cameras is $\approx 18,000$ square arcseconds, and would require 30 million exposures to cover the entire sky. In the individual ecliptic latitude bins, the total reservoirs of objects implied are $255,000 \pm 27,000$ asteroids within 10° of the ecliptic, $46,000 \pm 16,000$ between 10 and 25° of the ecliptic, and $12,000 \pm 7000$ above 25° of the ecliptic.

Figure 11 is a plot of the cumulative distribution of the HST asteroids vs apparent visual magnitude. It shows a steadily increasing asteroid population until about magnitude 23, where the curve begins to turn over. This is either due to incompleteness of the sample at the faintest magnitudes, or a real turnover in the size distribution. Ignoring those asteroids with apparent magnitudes above 23, we plot in Figure 12 the cumulative distribution of the HST asteroids vs absolute visual magnitude, H . Figure 12 is split into panels that correspond to the three semi-major axis ranges analyzed in the Palomar-Leiden survey (van Houten *et al.* 1970). We use the solar distances of our asteroids since the actual semi-major axes are not available, and assume that relatively few objects would cross bins in the course of their orbits.

If we assume that the number of asteroids in an absolute magnitude range that are imaged accidentally by the HST is related to the population density in that range, then we find that the cumulative population can be fit (loosely) by a power law of log cumulative number vs. absolute magnitude (H) to compare with other studies. Our fits to the slopes in Figures 12a, 12b and 12c are,

$$\log(N(H > H_0)) \propto 0.219 * \log(H_0), \quad 2 < a < 2.6AU$$

$$\log(N(H > H_0)) \propto 0.253 * \log(H_0), \quad 2.6 < a < 3AU$$

$$\log(N(H > H_0)) \propto 0.285 * \log(H_0), \quad 3 < a < 3.5AU$$

These power law coefficients can be compared to those derived from Table 5 of van Houten *et al.* (1970), 0.575, $2 < a < 2.6$; 0.449, $2.6 < a < 3$; and 0.436, $3 < a < 3.5$ (shown on Figures 12a-c). Our results differ not only in their reduced overall slopes, but also in that we find a growth in the slope as the semi-major axis increases. There is still a roll-over in the slope for brighter absolute magnitudes in these data after the asteroids with apparent magnitude greater than 23 (incomplete) are removed. Our findings indicate continued growth of the population of asteroids to that magnitude limit, but at a reduced slope.

Our orbital constraints on the inclinations of these asteroids are not restrictive enough to make comparisons of inclination versus size. To compare their distribution with the known asteroids, a sampling of specific epochs was chosen and the distribution of ecliptic latitude of 6213 numbered asteroids was compared to the ecliptic latitude of our sample. We find that $83.8 \pm 4\%$ of the numbered asteroids are contained within $\pm 10^\circ$ of the ecliptic for random epochs over a 10 year period. Figure 13 shows the heliocentric ecliptic latitude for the 52 asteroid trails with well measured distances; 87% of these objects were within $\pm 10^\circ$ of the ecliptic. We cannot show that our sample of relatively small asteroids exhibits the anti-equipartition of energy behavior seen previously (Mikami and Ishida 1987; Mikami *et al.* 1990) but improved detection statistics and sky coverage might allow this effect to be seen in the future.

b). Trojans

There are no clear detections of Trojan asteroids in our data set. There were 466 observations within 10 degrees ecliptic longitude and 25 degrees ecliptic latitude of the Jupiter L4 or L5 points, and thus are suitable fields to search for Trojan objects. Our main belt-detection statistics suggest that 10–15 foreground objects should appear in these fields. We found 11 objects, and 9 of these have distances and/or motions which place them in the main belt. The remaining two objects have no distance solution; u2e68c01t3 is a single bright (magnitude 19.8) straight trail and u27rgd01t2 is from two short 130 second exposures. An asteroid in a Jupiter Trojan orbit will appear about 3.5 mag fainter than a similar object in the main belt. HST's sensitivity to Trojans is thus limited to objects with absolute magnitudes, $H < 16$. If Trojans were distributed in our ecliptic coordinate bins with a density per square arcsec equal to main belt objects, and if they had the same magnitude distribution as seen here for main belt objects, then we would have expected to randomly find 4 Trojan asteroids in the selected fields. About 23 objects should have been detected if Trojans are as numerous as main-belt objects (Hughes and Harris 1994, Shoemaker, *et al.* 1992).

VI. Conclusions

1. Serendipitous observations of asteroids in long exposure Hubble Space Telescope images can add to the statistics on main-belt asteroids in the size range of 0.3 to 3 km.
2. The orbital motion of the HST Observatory induces a time-varying parallax which results in a unique curvature in the asteroid trails. Fitting of the trail shapes allows accurate determinations of an object's distance and absolute magnitude, and constrains some of the orbital parameters.
3. We find continued growth of the population of asteroids for smaller sizes. We find that the slope of the cumulative absolute magnitude distribution follows an approximate power law $N \propto H_0^{0.25}$ over the range $13 < H_0 < 16$ magnitude. This is a smaller slope than found in the Palomar-Leiden survey and others. Statistics of these finds imply a reservoir of $3.1 \times 10^5 \pm 6 \times 10^4$ asteroids of this size range within 25° of the ecliptic.

The results presented here do not represent the limit of what HST can accomplish in detection of main belt objects. HST/WFPC2 can reach down to visual point source magnitudes of 28 in a full orbit of observations; this corresponds to a ballpark diameter of 40m for a C type object at opposition at the inner edge of the main belt. Objects this small have not been detected in this study for two reasons: 1) the exposures times are typically half an orbit or less, and 2) the asteroid's light is typically spread over more than 50 pixels in each trail. The latter effect adds enough read noise to reduce photometric sensitivity by at least 3 magnitudes. Objects in the 25–60m size range (absolute magnitude 25.0) could be detected in the asteroid belt if dedicated HST observations were made using moving target tracking to keep asteroids at the desired distance as close to point sources as possible. This technique has been applied to searches for Kuiper belt objects (Cochran *et al.* 1995), but has not yet been done for main belt objects.

Acknowledgements

The Authors would like to thank Brian Marsden and Gareth Williams for help in identifying and checking our work on some of these objects and Eleanor Helin and David Rabinowitz for helpful discussions.

This work is being carried out at the Jet Propulsion Laboratory, California Institute of Technology, under contract NAS7-918 with the National Aeronautics and Space Administration.

References

- C.H. Acton, *Planet Space Sci.* 44, 65 (1996).
- E. Bowell, K. Lumme 1979, *Colorimetry and Magnitudes of Asteroids*, in *Asteroids* (T. Gehrels, ED.), pp 132-169. The University of Arizona Press, Tucson..
- E. Bowell, K. Muinonen, and L. H. Wasserman 1994. A public-domain asteroid orbit database. In "Asteroids, Comets, Meteors 1993" (A. Milani et al., eds.), pp. 477-481. under NASA grant NAGW-1470.
- A. Cellino, V. Zappala, P. Farinella, *The Size Distribution of Main-belt from IRAS Data*, *Royal Astronomical Society, Monthly Notices*, vol. 253, Dec. 15, 1991, p. 561-574.
- C. R. Chapman, K. Klaasen, M. J. S. Belton, J. Veverka 1994, *Asteroid 243 IDA and its satellite*, *Meteoritics*, vol. 29, no. 4, p. 455, 7/1994.
- A. L. Cochran, H. F. Levison, S. A. Stern, M. J. Duncan 1995, *The Discovery of Halley-sized Kuiper Belt Objects Using the Hubble Space*, *Ap. J.*, v.455, p.342, 12/1995.
- J. Donnison, R. Sugden 1984, *The Distribution of Asteroid Diameters*, *Royal Astronomical Society, Monthly Notices* vol. 210, Oct. 1, 1984, p. 673-682..

- P. Farinella, M. Carpino, CH. Froeschle, CL. Froeschle, R. Gonczi, The ages of asteroid families, *Astronomy and Astrophysics* (ISSN 0004-6361), vol. 217, no. 1-2, June 1989, p. 298-306..
- L. Frank, J. Sigwarth, J. Craven, *Geophysical Research Letters*, 13, 303, 1986..
- M. Gaffey, J. Bell and D. Cruikshank, 1989, Asteroid Surface Mineralogy, in *Asteroids II* (R. Binzel, T. Gehrels, M. Matthews ED.), pp 98-127. The University of Arizona Press, Tucson..
- Gehrels, T., McMillan, R.S., Rabinowitz, D.L. 1992. Automated Detection of Asteroids in Real-Time with the Spacewatch Telescope. In *Asteroids, Comets, and Meteors 1991*, eds. A. Harris and E. Bowell (Houston: Lunar and Planetary Inst.), pp. 541-544..
- C. van Houten, I. van Houten-Groeneveld, P. Herget and T. Gehrels, The Palomar-Leiden Survey of Faint Minor Planets, *Astronomy and Astrophysics Supplement*, V2, No.5, 10/1970.
- D. Hughes 1982, Asteroid Size Distribution, *Monthly Notices of the Royal Astronomical Society*, v199, pp1149-1157 (1982).
- D. Hughes and N. Harris, 1994, The Distribution of Asteroid Sizes and its Significance, *Planetary and Space Science*, vol. 42, no. 4, p. 291-295 4/1994.
- WFPC2 Instrument Handbook, <http://www.stsci.edu/instruments.html>.
- T. Mikami, K. Ishida 1987, Segregation of Asteroids with Different Sizes for Kinematic Properties, *Astronomical Society of Japan, Publications* vol. 39, no. 2, 1987, p. 361-373..
- Mikami, Takao, Ishida, Keiichi 1990, Size distributions of member asteroids in seven Hirayama families, *Astronomical Society of Japan, Publications*

vol. 42, no. 1, 1990, p. 165–174..

- E. Shoemaker, C. Shoemaker, R. Wolfe, Trojan asteroids – Populations, dynamical structure and origin of the L4 and L5 swarms, in Asteroids II (R. Binzel et al., ED.), pp 487–523. The University of Arizona Press, 1989.
- A. L. Whipple, P. J. Shelus, R. W. Whited, A. L. Cochran, P. J. Macqueen, G. F. Benedict 1995, McDonald Observatory Solar System Object Astrometry from Wide Field CCD Imaging, Bull. American Astron. Soc., 187, No.42.02 12/1995.
- M. M. Waldrop, Operation Spacewatch, SCIENCE, vol. 216, 42, 1982 .
- S. Xu, R. Binzel, T. Burbine, S. Bus 1995, Small Main–belt Asteroid Spectroscopic Survey: Initial Results, Icarus vol. 115, no. 1, p. 1–35 5/95.
- M. Yuasa, 1983, On the ages of asteroid families, in “Dynamical trapping and evolution in the solar system; Proceedings of the Seventy–fourth Colloquium”, Gerakini, Greece, August 30–September 2, 1982 (A84–34976 16–89). Dordrecht, D. Reidel Publishing Co., 1983, p. 203–210.

Figure Captions

Figure 1. Sky coverage in Earth ecliptic coordinates. Shown are the positions in the sky for each HST exposure examined for asteroid trails. The area of each dot is proportional to the number of images taken in a 1 x 1 degree patch of sky, not the physical area of the sky covered. The area marked HDF is the Hubble Deep field.

Figure 2. Asteroid u2805m01t4, a magnitude 18.7 object that is imaged only once by HST/WFPC2 (blue frame). In the next exposure (red frame) the asteroid has already left the field of view to the upper right. To complete the color image, both red and blue frames are reproduced in green. These frames are raw images.

Figure 3. Asteroid u2b40502t4, a magnitude 21.7 object is photographed in four frames in two consecutive HST orbits. The asteroid enters the field to the right in the first exposure giving an incomplete trail. The second exposure shows a complete trail plus an earth-orbiting satellite. In the next orbit, HST captures two complete trails of the asteroid. These are raw images except the second set of trails are cut and pasted to the first two images to prevent an excessive number of cosmic ray tracks in each color plane.

Figure 4. Asteroid u27rf401t3 in a 200 X 200 pixel area of an image. This last object is a magnitude 23 (V) asteroid. There are dimmer examples but they are hard to reproduce in a graphic. Difficulties of detecting and doing photometry on dim asteroid trails should be apparent

Figure 5. Distance solution for asteroid u2805m01t4 seen in figure 1. At the top is a plot of χ^2 vs the Earth-asteroid separation showing a minimum at .93 A.U. At the bottom is a plot of data (open and filled circles) and model (solid lines) trails. Fits are shown for Earth distances of 0.4, 0.55, 0.93 and 2.5 A.U. The fit for 0.93 A.U is not labeled but goes through the points. This is a potential Mars-crosser found at a heliocentric distance of 1.67 A.U., identical to Mars' aphelion distance. The fit is excellent because of the length and curvature of the trail.

Figure 6. Distance solution to asteroid u2b40401t3 seen in three orbits of HST. At

the top is a plot of χ^2 vs the Earth–asteroid distance showing the minimum at 1.48 A.U. At the bottom is a plot of data (open and filled circles) and model (solid line) trails. This is a magnitude 22 object which at a heliocentric distance of 2.36 A.U., is an inner main belt asteroid. The uncertainty in the derived distance is very small due to the length and complexity of the trail. The lower trail at the bottom is broken up because distant galaxy images overlay the trail.

Figure 7. Distance solution to asteroid u26g0e02t4. At the top is a plot of χ^2 vs the Earth–asteroid distance showing the minimum at 1.70 A.U. The broad well shows that this is a poorer fit; little or no curvature in the trail (seen at bottom) can confuse the solution.

Figure 8. Distance solution to asteroid u26g0601t4. The first exposure is 1500 seconds and the last is 900 seconds. The asteroid is moving retrograde during the exposures and makes a prograde loop between exposures as HST rounds the Earth. The derived distance is excellent because of the complexity of the trail seen in the bottom panel. The break in the longer trail right before the two cross is from a large cosmic–ray hit on the CCD. This trail is probably to be identified with asteroid 1992 UY3.

Figure 9. Distance to 52 asteroids that have good distance solutions. Since the orbital elements are not completely determined the semi–major axis is not plotted here. Still, it is apparent that the asteroid belt is well represented.

Figure 10. Orbital families consistent with asteroid u2b40401t3's solution. Eccentricities vs semi–major axis is shown by the solid line and inclination vs semi–major axis is shown by the dashed line. The left label is eccentricity and the right label is inclination.

Figure 11. Cumulative number of asteroids found vs apparent visual magnitude for HST detected asteroids.

Figure 12. Cumulative growth of population vs absolute magnitude for 52 HST asteroids. Figure 12a, b and c are for asteroids with solar distance $2 < r < 2.6$, $2.6 < r < 3$ and $3 < r < 3.5$ respectively for comparison with the Palomar–Leiden surveys shown as the

upper plot. Semi-major axis ranges of $2 < a < 2.6$, $2.6 < a < 3$ and $3 < a < 3.5$. A size scale is appended to the top of each graph that correspond to an albedo of 0.15 (S-type asteroid). An error bar corresponding to change in albedo is shown at top left.

Figure 13. Heliocentric ecliptic latitude of 52 asteroids found. The other asteroids did not have a distance solution and so cannot be presented here even though the ecliptic latitude is known.

Special symbols used

α	= <code>\alpha</code>
$\dot{\alpha}$	= <code>\dot{\alpha}</code>
α_0	= <code>\alpha_0</code>
Δ	= <code>\Delta</code>
Δ_{max}	= <code>\Delta_{\{max\}}</code>
δ	= <code>\delta</code>
$\dot{\delta}$	= <code>\dot{\delta}</code>
δ_0	= <code>\delta_0</code>
\cdot	= <code>\cdot</code>
χ^2	= <code>\chi^2</code>
π	= <code>\pi</code>
\pm	= <code>\pm</code>
\circ	= <code>\circ</code>
\propto	= <code>\propto</code>
\approx	= <code>\approx</code>
$'$	= <code>\prime</code>
$''$	= <code>\prime\prime</code>
$\%$	= <code>\%</code>
\vec{P}	= <code>\vec{\bf P}</code>

TABLE 1
Asteroid Trail Observations

IMAGES	FILTER MAG
u23t0204t3	F702W <21.53
u2680103t4, u2680104t4	F555W 20.79
u2690l02t2	F555W <22.66
u26g0601t4, u26g0602t4	F555W 18.95
u26g0901t2	F555W 21.30
u26g0d01t4	F555W 20.02
u26g0e01t3	F555W 22.03
u26g0e02t4, u26g0e03t4	F555W 22.12, F814W 21.54
u26g0q01t2, u26g0q02p2	F555W 21.33
u26k0p01t3, u26k0p02t3, u26k0p02t2	F814W 21.28
u26k0u01t3, u26k0u02t3	F814W 21.25
u26kqr01t4	F814W 19.74
u27rbr01t4, u27rbr02t4	F814W 23.40
u27rdd01t3, u27rdd02t3	F814W 22.12
u27rf401t3, u27rf402t3	F814W 22.46
u27rgd01t2, u27rgd02t2	F814W 21.13
u27yg701t3, u27yg702t3	F814W 19.21
u27z6501t3, u27z6502t3, u27z5601t3	F606W 18.63, F814W 18.36
u27z7103t3	F814W 22.32
u27z7601t2, u27z7601t3, u27z7602t3	F606W 22.51 F814W 22.33
u2802t01t2, u2802t02t2	F606W 21.66 F814N 21.40
u2803y01t4, u2803y02t4, u2803y02t3	F606W 21.30 F814W 22.51
u2803z01t3, u2803z02t3	F606W 21.30 F814N 21.05
u2804o01t3, u2804o02t3	F606W 22.59 F814W 22.18
u2804r02t3	F814N 19.91
u2805a01t2, u2805a02t2	F606W 20.17 F814N 19.86
u2805m01t4	F606W 18.73
u2805u01n4, u2805u02t4	F606W 21.83 F814N 21.63
u2805v01t2, u2805v02t2	F606W <18.93 F814N 18.22
u2805x01t2	F606W 23.52
u2805x01t2	F606W 23.32
u2806b01t4, u2806b02t4	F606W 21.53 F814N <21.49
u280fq01t4, u280fq02t4	F606W 20.73 F814N 20.30

TABLE 1 (continued)
Asteroid Trail Observations

IMAGES	FILTER MAG
u280fr01t4, u280fr02t4	F606W 21.47 F814N 21.24
u280fr02t2	F814N 23.45
u280fv01t3, u280fv02t3	F606W 20.71 F814N 20.68
u280g201t3	F606W —
u2880103t4, u2880104t4, u2880105t4, u2880106t4, u2880107t4, u2880108t4	F814W 21.30
u28e0101t4, u28e0102t4, u28e0103t4, u28e0104t4	F555W 21.39
u2ar0903t4	F606W 22.53
u2ar0c01t3, u2ar0c02t3, u2ar0c03t3	F606W 21.50
u2ar0c03t2, u2ar0c03t3	F606W 20.74
u2av0101t4, u2av0102t4, u2av0103t4, u2av0104t4	F702W 23.91
u2av0301t4, u2av0302t4, u2av0303t4, u2av0304t4	F702W 23.04
u2b40401t3, u2b40402t3, u2b40403t4, u2b40404t1, u2b40405t1	F814W 21.56
u2b40502t4, u2b40503t4, u2b40504t4, u2b40505t4	F814W 21.40
u2c4090ct2	F555W 22.36
u2ck0d04t3, u2ck0d05t3, u2ck0d07t3, u2ck0d08t3, u2ck0d09t3, u2ck0d0at3	F555W 22.35
u2e61301t2	F606W 22.57
u2e61p01t4	F606W 17.30
u2e63h01t3	F606W 23.18
u2e65d01t4	F606W 22.63
u2e66501t2	F606W 21.99
u2e66901t3	F606W 22.71
u2e66l01t4	F606W 20.87
u2e67y01t4	F606W 22.38
u2e68c01t3	F606W 19.82
u2e68j01t4	F606W 21.21
u2eb0101t3, u2eb0102t3	F702W 21.29
u2eb0101t4, u2eb0102t4	F702W 22.60
u2eb0201t4, u2eb0202t4	F702W 23.06
u2ek0606t3	F675W <21.64
u2fl0103t2	F675W < 21.48
u2fs0401n4, u2fs0402p4, u2fs0403p4	F702W 22.99
u2gx0201t2, u2gx0202t2	F622W 22.67
u2gx040nt2, u2gx040ot2	F675W 20.70
u2gx0607t2, u2gx0608p2	F622W 21.53

TABLE 1 (continued)
Asteroid Trail Observations

IMAGES	FILTER MAG
u2gx070dn4, u2gx070et4	F675W 22.52
u2he030ft2	F814W 21.21
u2hn010cp2, u2hn010dp2, u2hn010en2, u2hn010ft2	F606W 22.70
u2hn0108p2, u2hn0109p3, u2hn010ap3, u2hn010bp3, u2hn010cp3, u2hn010dp3, u2hn010en3, u2hn010ft3	F606W 22.25
u2hn0301t4, u2hn0302t4, u2hn0303t4, u2hn0304t4, u2hn0305t4, u2hn0306t4, u2hn0307t4	F606W 23.55
u2hn040gt4, u2hn040ht4, u2hn040it4, u2hn040jt4	F606W 22.85
u2hn0404t3, u2hn0405t3, u2hn0406t3, u2hn0407t3, u2hn0408t4, u2hn0409t4, u2hn040at4, u2hn040bt4	F606W 22.44
u2hn0404t3, u2hn0405t3, u2hn0406t2, u2hn0407t2, u2hn0408t2, u2hn0409t2, u2hn040at2, u2hn040bt2, u2hn040cm2 u2hn040dt2 u2hn040et2	F606W 21.78
u2l50801t4, u2l50802t4	F814W 20.08
u2om1201t4, u2om1202t4, u2om1203t4, u2om1204t4	F702W 16.61
u2oo0401t2, u2oo0401t2, u2oo0402t2, u2oo0403t2	F300W 17.26 F380W 16.16 F791W 16.13
u2os0701t3	F814W 22.72
u2ot0q01t4	F814W 21.73
u2ov2j01t3, u2ov2j02t3, u2ov2j03t3	F814W 20.48
u2ov2j01t2, u2ov2j02t2, u2ov2j03t2 u2ov2j04t2	F814W 22.97
u2ov5601t2, u2ov5602t2	F814W 20.66
u2ov5d01t3, u2ov5d02t3	F606W 22.15
u2ov6f01t4, u2ov6f02t4, u2ov6f03t4, u2ov6f04t4	F814W 23.38
u2ov7t01t4, u2ov7t02t4, u2ov7t03t4, u2ov7t04t4	F814W 21.28
u2ov9w01p2, u2ov9w02p2, u2ov9w03p2, u2ov9w04p2	F814W 22.06
u2ova001t4, u2ova002t4	F606W 22.61
u2ovab01t2, u2ovab02t2, u2ovac01t2, u2ovac02t2	F606W 23.84 F814W 22.42
u2rk0201t4, u2rk0202t4, u2rk0203t3	F785LP 22.02 F702W 21.11
u2rk0801t4, u2rk0802t4	F785LP 21.24
u2sw0501t1, u2sw0502t4	F606W 23.64
u2sw0502t4 other	F606W bright
u2w90701t1, u2w90702t1	F606W 22.31
u33l3801m3, u33l3802m3	F814W 19.77
u3800201t1, u3800201t2, u3800201t3, u3800201t4	F410M 17.60
u3b80l01t2, u3b80m01t2	F814W 21.37 F606W 20.68

TABLE 2
Asteroid Distances and Derived Quantities

IMAGE NAME	Earth Distance (AU)	Solar Distance (AU)	CHISQ OF FIT	H	Radius (km)
u26g0601t4	1.92 +0.06 -0.05	2.63 +0.05 -0.05	0.18	14.4	2.2
u26g0901t2	3.14 +0.81 -0.34	3.20 +0.77 -0.32	1.04	16.3	0.9
u26g0d01t4	1.94 +0.37 -0.11	1.74 +0.33 -0.09	2.03	16.7	1.0
u26g0e02t4	1.70 +0.37 -0.24	2.60 +0.36 -0.24	0.74	18.5	0.3
u26g0q01t2	2.20 +0.47 -0.61	3.03 +0.46 -0.61	0.30	16.4	0.9
u26k0p01t3	2.25 +0.22 -0.20	3.20 +0.22 -0.20	1.78	16.6	0.8
u26k0u01t3	1.97 +0.05 -0.05	2.84 +0.04 -0.04	2.32	16.8	0.8
u27rf401t3	2.25 +0.94 -0.51	3.24 +0.94 -0.51	1.16	18.3	0.4
u27z5601t3	2.46 +0.10 -0.04	2.76 +0.09 -0.03	0.57	13.7	3.2
u27z7601t2	2.48 +0.03 -0.01	2.69 +0.02 -0.01	3.81	17.5	0.5
u2802t01t2	1.64 +0.92 -0.43	2.63 +0.91 -0.42	0.23	18.3	0.4
u2803z01t3	2.61 +0.33 -0.26	2.71 +0.31 -0.24	0.72	15.9	1.2
u2805a01t2	1.82 +0.29 -0.22	2.20 +0.26 -0.19	0.57	15.9	1.1
u2805m01t4	0.93 +0.03 -0.03	1.68 +0.03 -0.03	0.96	16.4	0.9
u2805u01t4	3.15 +0.34 -0.34	3.35 +0.33 -0.32	0.26	15.8	1.2
u2805v01t2	2.51 +0.24 -0.19	2.46 +0.22 -0.19	0.33	13.6	3.3
u2806b01t4	2.88 +0.13 -0.10	2.85 +0.12 -0.09	0.69	16.0	1.1
u280fq01t4	1.87 +0.08 -0.07	2.86 +0.08 -0.07	0.42	16.9	0.7
u280fr01t4	2.65 +0.19 -0.17	3.64 +0.19 -0.17	0.53	16.5	0.8
u280fv01t3	2.17 +0.69 -0.42	2.65 +0.69 -0.42	0.19	15.9	1.1
u2880103t4	2.02 +0.03 -0.02	2.50 +0.02 -0.02	3.42	18.1	0.4
u28e0101t4	2.73 +0.05 -0.04	3.06 +0.05 -0.04	0.80	17.1	0.6
u2ar0903t4	2.30 +0.43 -0.31	3.30 +0.42 -0.31	0.79	18.2	0.4
u2ar0c01t3	1.72 +0.17 -0.17	2.72 +0.17 -0.17	0.56	18.2	0.4
u2ar0c03t3	1.91 +0.15 -0.13	2.91 +0.15 -0.12	0.56	16.8	0.8
u2b40401t3	1.49 +0.01 -0.01	2.37 +0.01 -0.01	1.63	18.2	0.4

TABLE 2 (continued)
Asteroid Distances and Derived Quantities

IMAGE NAME	Earth Distance (AU)	Solar Distance (AU)	CHISQ OF FIT	H	Radius (km)
u2b40502t4	2.15 +0.10 -0.10	3.02 +0.10 -0.09	0.32	17.0	0.7
u2ck0d04t3	2.74 +0.04 -0.05	3.47 +0.04 -0.04	0.48	16.4	0.8
u2fs0401t4	2.34 +0.12 -0.11	3.19 +0.11 -0.11	0.42	18.0	0.4
u2gx040nt2	2.46 +0.36 -0.23	2.66 +0.34 -0.21	0.43	15.6	2.3
u2gx0607t2	2.57 +0.35 -0.18	2.21 +0.32 -0.17	2.29	16.8	0.7
u2hn0108t2	2.46 +0.07 -0.06	2.68 +0.07 -0.05	0.95	17.4	0.6
u2hn010ct2	2.92 +0.29 -0.25	3.11 +0.29 -0.25	1.84	16.9	0.7
u2hn0301t4	2.43 +0.05 -0.01	2.57 +0.04 -0.01	2.43	18.5	0.3
u2hn0404t3	2.60 +0.19 -0.14	2.72 +0.17 -0.13	0.46	17.2	0.6
u2hn0405t3	3.13 +0.27 -0.23	3.22 +0.26 -0.22	0.39	15.8	1.2
u2hn040gt4	2.08 +0.00 -0.37	2.24 +0.00 -0.32	1.33	18.3	0.4
u2l50801t4	2.50 +0.10 -0.10	2.30 +0.10 -0.09	2.67	15.8	1.2
u2om1201t4	0.96 +0.02 -0.02	1.91 +0.02 -0.02	2.44	14.4	2.2
u2ot0q01t4	2.74 +0.06 -0.11	2.94 +0.06 -0.10	4.37	16.3	1.6
u2ov2j01t3	2.19 +0.27 -0.22	2.38 +0.24 -0.20	1.44	15.8	1.2
u2ov5601t2	1.99 +0.33 -0.24	1.87 +0.29 -0.20	0.28	16.3	0.9
u2ov5d01t3	3.29 +0.16 -0.16	3.03 +0.15 -0.15	0.95	16.2	1.7
u2ov6f01t4	2.16 +0.43 -0.01	2.72 +0.44 -0.01	1.12	18.4	0.4
u2ov7t01t4	2.12 +0.15 -0.10	2.43 +0.13 -0.09	0.53	16.7	0.8
u2ov9w01t2	1.71 +0.06 -0.06	2.69 +0.06 -0.06	0.62	18.7	0.3
u2ova001t4	1.88 +0.16 -0.20	2.05 +0.14 -0.17	1.01	18.4	0.4
u2ovab01t2	2.88 +0.09 -0.07	2.84 +0.09 -0.06	2.16	17.3	0.6
u2sw0502t4	1.91 +0.05 -0.05	2.78 +0.04 -0.04	0.89	19.3	0.4
u2w90701t1	2.13 +0.25 -0.19	2.99 +0.24 -0.19	0.17	17.6	0.5
u33l3801m3	0.71 +0.04 -0.03	1.65 +0.03 -0.03	3.72	18.3	0.6
u3800201t3	1.89 +0.05 -0.05	2.84 +0.05 -0.05	3.26	15.3	2.5

TABLE 3
Asteroids without good fits

IMAGE NAME	Earth Distance (AU)	CHISQ OF FIT	GEOCENTRIC ECLIPTIC LATITUDE	NOTE
u23t0204t3	—	—	31.2	moves off CCD
u2680103t4	2.62 +0.40 -0.19	7.44	0.03	straight track
u2690l02t2	—	—	5.4	moves off CCD
u26g0e01t3	2.73 +3.97 -1.35	0.36	5.9	straight track
u26kqr01t4	1.62 +5.08 -1.00	0.12	-5.6	straight track
u27rbr01t4	6.70 +0.00 -0.26	29.7	7.1	straight track
u27rdd01t3	3.43 +3.27 -0.20	1.11	3.3	straight track
u27rgd01t2	6.70 +0.00 -5.70	0.57	3.0	straight track
u27yg701t3	6.70 +0.01 -4.97	0.07	0.9	straight track
u27z7103t3	2.48 +0.28 -0.23	10.3	-8.7	straight track
u2803y01t4	2.42 +2.42 -1.03	1.49	-6.5	straight track
u2804o01t3	3.17 +1.72 -0.60	1.48	-5.9	straight track
u2804r02t3	2.44 +4.26 -2.22	0.44	-7.6	straight track
u2805x01t2	1 —	—	-7.9	straight track
u2805x01t2	2 —	—	-7.9	straight track
u280fr02t2	tumbling space junk?	—	-0.4	straight track
u280g201t3	—	—	1.1	moves off CCD
u2av0101t4	—	—	-0.5	SL-9 tracking
u2av0301t4	—	—	-0.5	SL-9 tracking
u2c4090ct2	tumbling space junk?	—	-73.7	straight track
u2e61301t2	—	—	3.4	straight track

TABLE 3
Asteroids without good fits

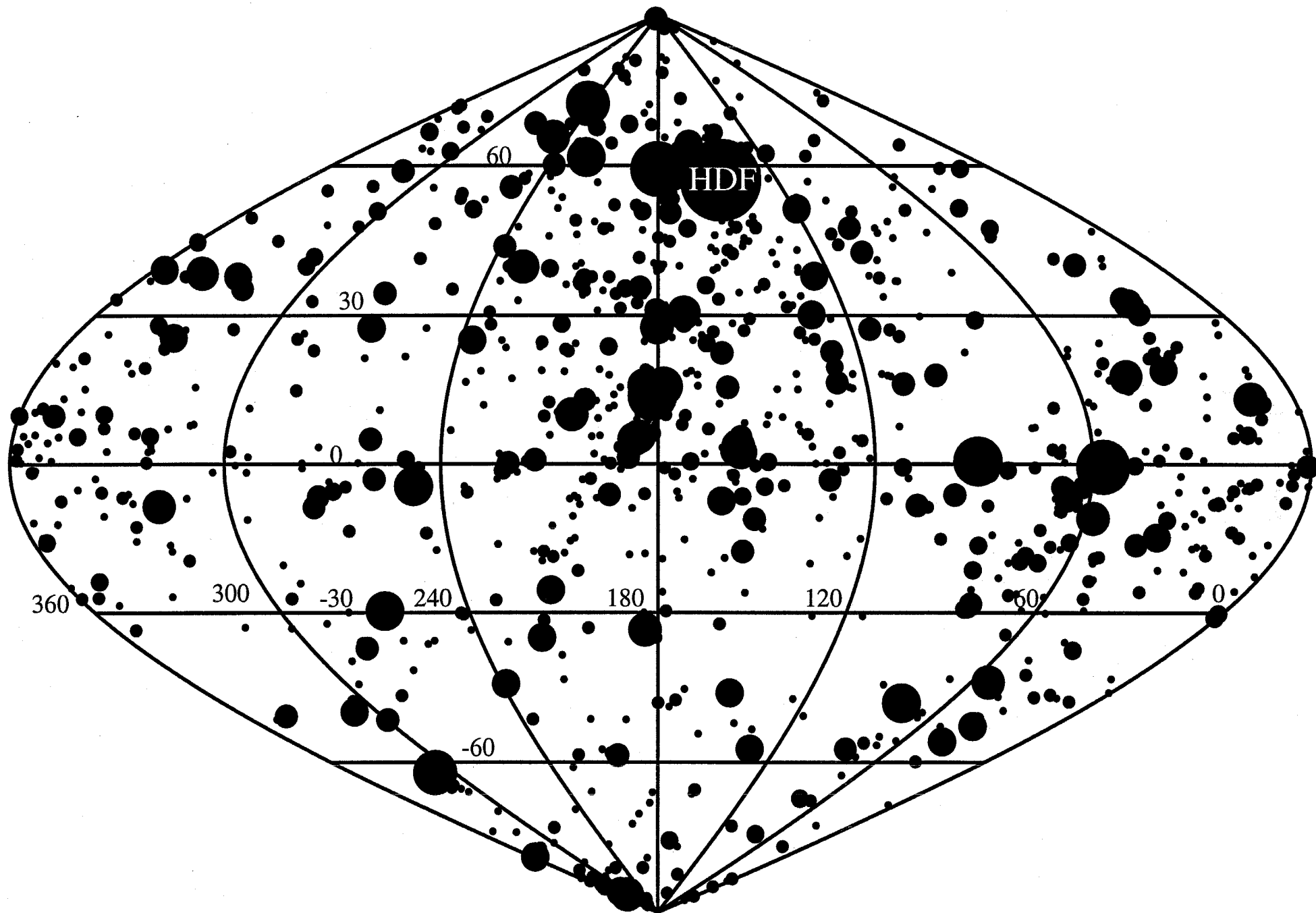
IMAGE NAME	Earth Distance (AU)	CHISQ OF FIT	GEOCENTRIC ECLIPTIC LATITUDE	NOTE
u2e61p01t4	3.03 +3.66 -1.42	0.13	15.7	straight track
u2e63h01t3	6.70 +0.00 -6.31	0.36	-5.3	straight track
u2e65d01t4	1.77 +4.93 -0.85	1.24	10.6	straight track
u2e66501t2	1.82 +4.88 -0.87	0.14	1.5	straight track
u2e66901t3	—	—	-21.7	straight track
u2e67y01t4	2.16 +2.62 -0.74	0.65	-4.1	straight track
u2e68c01t3	—	—	-5.3	straight track
u2e68j01t4	3.47 +3.23 -1.68	1.56	4.9	straight track
u2eb0101t3	—	—	-0.05	SL-9 tracking
u2eb0101t4	—	—	-0.05	SL-9 tracking
u2eb0202t4	—	—	-0.05	SL-9 tracking
u2ek0606t3	—	—	-4.9	moves off CCD
u2fl0103t2	—	—	13.4	moves off CCD
u2gx0201t2	3.54 +0.82 -0.52	0.81	-7.9	straight track
u2gx070dn4	—	—	3.7	straight track
u2he030ft2	2.77 +3.83 -1.65	0.38	-4.9	straight track
u2ov2j01t2	1.32 +0.07 -0.00	19.3	-0.2	straight track
u2rk0201t4	—	—	4.7	straight track
u2rk0801t4	—	—	3.9	straight track
u2sw0501t1	2 —	—	3.9	trail ends in star
u3b80l01t3	disjoint trails	—	6.2	image motion?

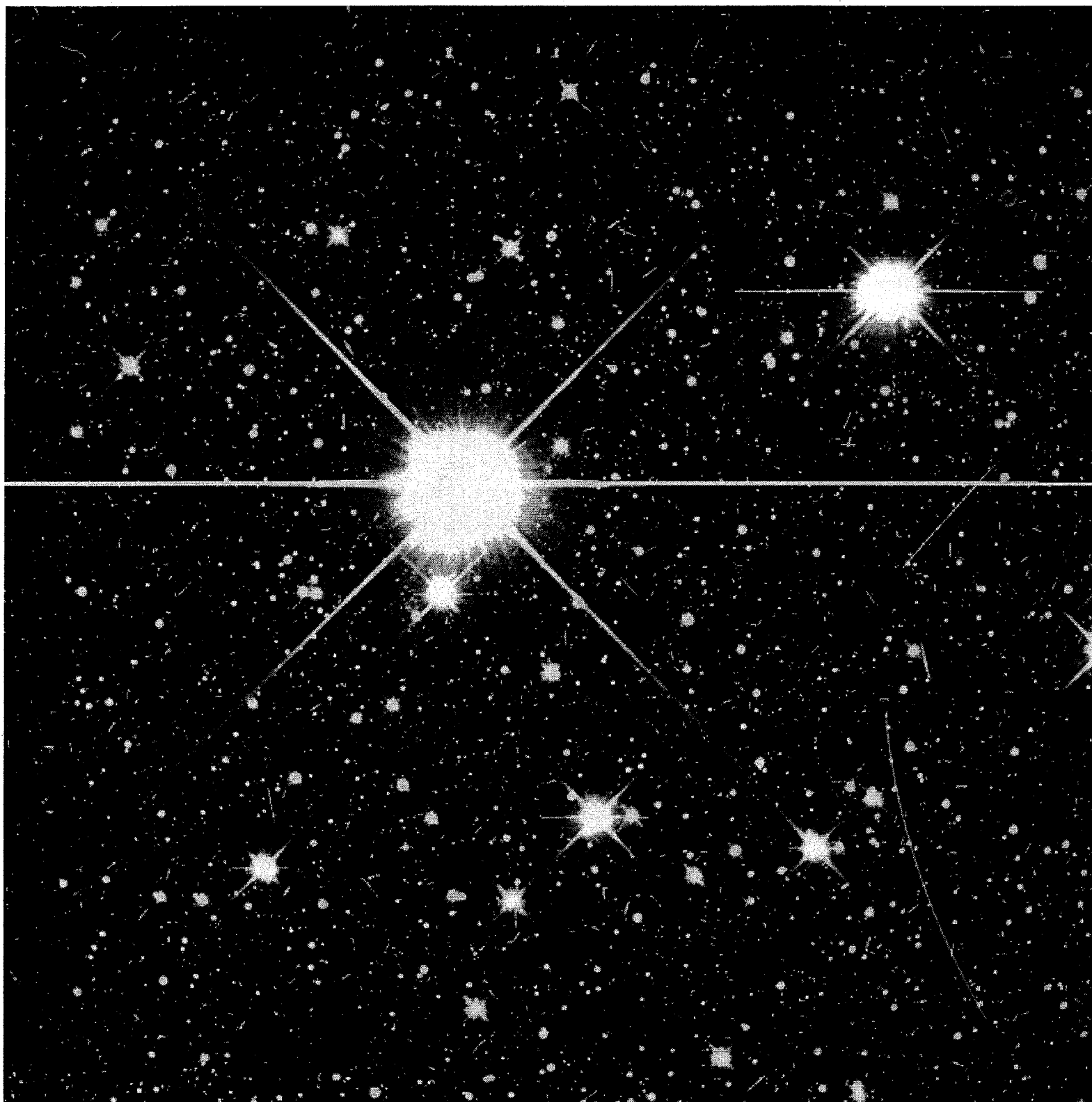
TABLE 4
Asteroid Motion and Derived Quantities

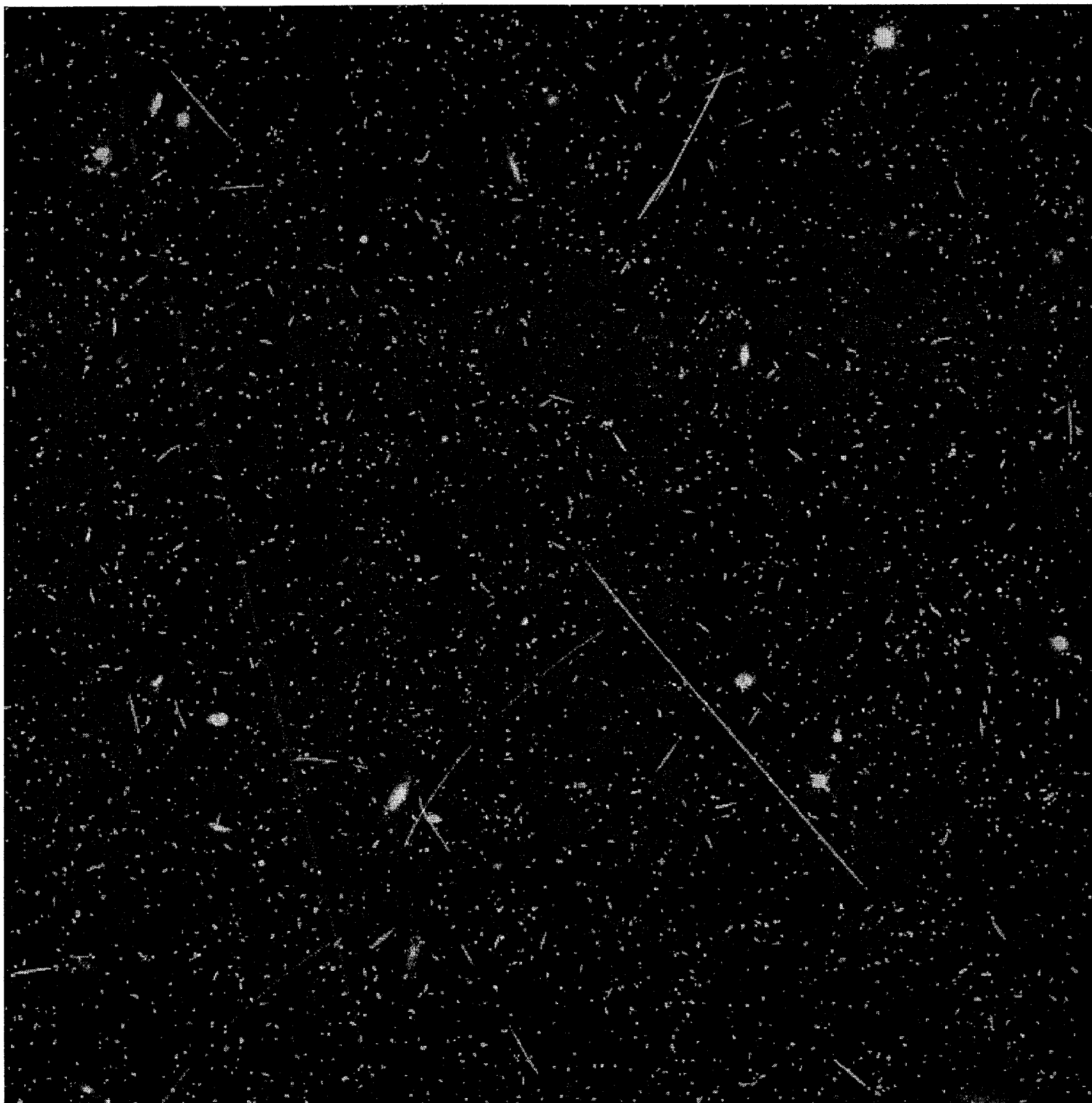
IMAGE NAME	Ecliptic Latitude (deg)	Geocentric Intrinsic RA rate (arcsec per hr)	Geocentric Intrinsic DEC rate (arcsec per hr)	ORBIT NOTES ORBIT NOTES
u26g0601t4	2.8	36.1 + 1.2 - 1.1	-17.2 + 0.4 - 0.4	a > 2.01, e > .02, 05.3 < i < 06.4
u26g0901t2	3.7	17.0 + 1.4 - 0.8	-13.0 + 0.1 - 0.1	a > 2.37, e > .24, 13.0 < i < 37.0
u26g0d01t4	4.2	32.3 + 3.4 - 1.3	-16.8 + 0.6 - 0.2	a > 1.08, e > .32, 04.3 < i < 160.
u26g0e02t4	3.8	44.4 + 15.4 - 15.7	-20.1 + 5.4 - 5.3	a > 2.12, e > .18, 04.0 < i < 06.3
u26g0q01t2	4.3	32.6 + 8.2 - 17.8	-17.6 + 4.2 - 9.1	a > 2.70, e > .08, 05.4 < i < 11.3
u26k0p01t3	5.5	35.3 + 5.7 - 6.1	-10.0 + 2.6 - 2.8	a > 3.01, e > .06, 07.5 < i < 11.0
u26k0u01t3	-20.4	39.3 + 1.3 - 1.4	-24.1 + 1.0 - 1.0	a > 2.63, e > .07, 20.3 < i < 27.1
u27rf401t3	2.1	34.2 + 22.3 - 22.0	7.2 + 0.2 - 0.2	a > 2.62, e > .04, 03.7 < i < 06.1
u27z5601t3	8.6	29.5 + 0.2 - 0.1	-5.6 + 0.4 - 0.2	a > 2.14, e > .15, 11.4 < i < 16.1
u27z7601t2	-1.3	31.2 + 0.1 - 0.1	-13.6 + 0.1 - 0.1	a > 2.27, e > .05, 05.6 < i < 14.7
u2802t01t2	-4.6	61.6 + 38.8 - 37.9	-3.4 + 1.6 - 1.5	a > 3.14, e > .16, 11.1 < i < 15.9
u2803z01t3	-5.1	34.1 + 1.4 - 1.3	2.6 + 1.3 - 1.2	a > 2.65, e > .07, 05.1 < i < 05.4
u2805a01t2	-3.2	44.2 + 3.3 - 3.2	22.3 + 2.2 - 2.1	a > 1.76, e > .05, 11.2 < i < 50.4
u2805m01t4	-23.0	115.8 + 5.2 - 5.6	-39.8 + 0.8 - 0.9	a > 0.99, e > .45, 23.0 < i < 83.1
u2805u01t4	-3.9	23.3 + 1.1 - 1.3	-3.2 + 0.7 - 0.9	a > 2.72, e > .14, 12.0 < i < 27.4
u2805v01t2	-4.4	32.7 + 0.2 - 0.2	5.6 + 0.3 - 0.2	a > 1.93, e > .11, 04.4 < i < 04.5
u2806b01t4	1.2	27.8 + 0.1 - 0.1	-2.3 + 0.2 - 0.2	a > 2.19, e > .17, 03.6 < i < 10.1
u280fq01t4	-0.5	45.7 + 3.6 - 3.3	-14.6 + 0.3 - 0.3	a > 2.64, e > .09, 18.8 < i < 19.6
u280fr01t4	-0.5	29.4 + 4.4 - 4.4	-0.8 + 0.4 - 0.4	a > 3.20, e > .14, 01.6 < i < 02.1
u280fv01t3	-3.4	36.6 + 9.5 - 9.1	6.9 + 0.4 - 0.4	a > 2.06, e > .14, 04.7 < i < 06.3
u2880103t4	3.7	39.3 + 0.3 - 0.2	-14.9 + 0.0 - 0.0	a > 2.06, e > .06, 03.7 < i < 04.5
u28e0101t4	-4.9	27.4 + 0.0 - 0.2	-7.9 + 0.0 - 0.1	a > 2.50, e > .12, 09.3 < i < 24.2
u2ar0903t4	10.2	30.4 + 11.0 - 11.0	-14.1 + 5.0 - 4.9	a > 2.99, e > .10, 10.2 < i < 12.3
u2ar0c01t3	-0.3	52.6 + 7.1 - 8.3	18.6 + 2.4 - 3.0	a > 2.95, e > .08, 00.7 < i < 00.9
u2ar0c03t3	0.3	40.4 + 6.4 - 6.4	23.1 + 1.6 - 1.6	a > 2.91, e > .00, 11.5 < i < 11.7
u2b40401t3	8.2	60.7 + 0.5 - 0.3	-21.8 + 0.3 - 0.1	a > 2.33, e > .04, 06.2 < i < 08.4

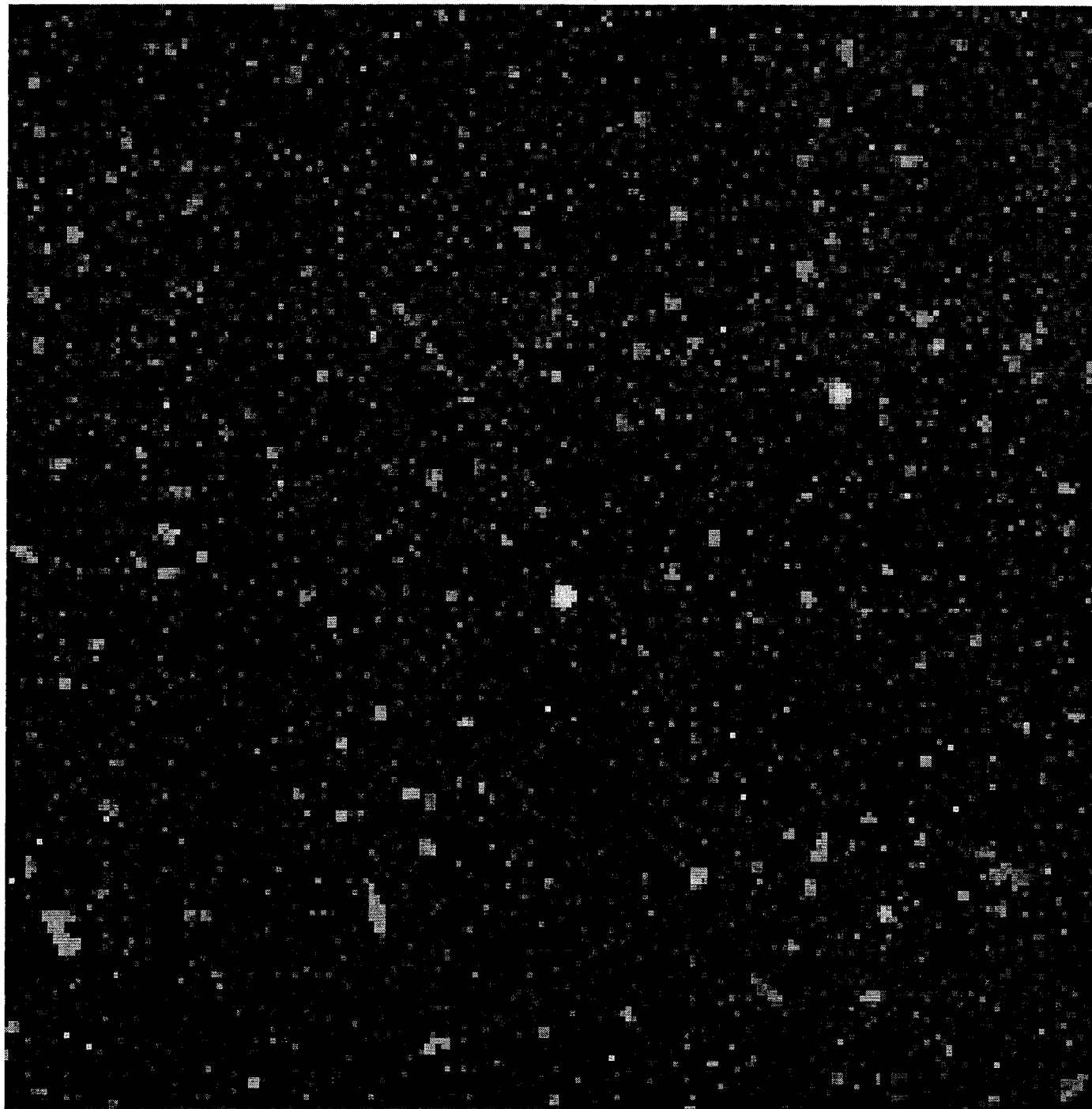
TABLE 4 (continued)
Asteroid Motion and Derived Quantities

IMAGE NAME	Ecliptic Latitude (deg)	Geocentric Intrinsic RA rate (arcsec per hr)	Geocentric Intrinsic DEC rate (arcsec per hr)	ORBIT NOTES ORBIT NOTES
u2b40502t4	7.1	33.5 + 2.3 - 2.4	-20.4 + 1.2 - 1.2	a > 2.99, e > .02, 08.6 < i < 16.3
u2ck0d04t3	11.4	20.0 + 0.5 - 0.5	-12.4 + 0.3 - 0.4	a > 2.56, e > .30, 11.4 < i < 19.6
u2e67y01t4	-4.1	30.4 + 25.2 - 25.1	-16.0 + 18.7 - 18.7	a > 2.34, e > .21, 04.4 < i < 10.5
u2fs0401t4	4.8	30.5 + 2.8 - 2.8	17.0 + 1.0 - 1.0	a > 3.11, e > .01, 06.5 < i < 12.4
u2gx040nt2	-2.6	33.7 + 1.8 - 1.4	-4.7 + 0.3 - 0.3	a > 2.22, e > .05, 05.5 < i < 16.4
u2gx0607t2	-4.4	31.9 + 2.1 - 1.4	-4.5 + 2.2 - 1.4	a > 1.67, e > .16, 08.8 < i < 26.5
u2hn0108t2	-0.04	34.7 + 0.1 - 0.1	-1.1 + 0.1 - 0.1	a > 2.22, e > .06, 10.8 < i < 31.2
u2hn010ct2	-0.04	27.6 + 1.1 - 1.2	-0.4 + 0.2 - 0.2	a > 2.64, e > .07, 10.5 < i < 24.8
u2hn0301t4	-0.04	33.8 + 0.2 - 0.0	5.2 + 0.1 - 0.1	a > 2.02, e > .11, 02.7 < i < 09.6
u2hn0404t3	-0.04	30.0 + 0.4 - 0.3	14.6 + 0.3 - 0.2	a > 2.37, e > .02, 10.5 < i < 27.9
u2hn0405t3	-0.04	24.1 + 0.4 - 0.4	8.3 + 0.3 - 0.3	a > 2.79, e > .05, 05.4 < i < 11.9
u2hn040gt4	-0.04	44.5 + 0.1 - 1.6	-16.5 + 0.1 - 1.7	a > 2.04, e > .04, 24.5 < i < 67.6
u2l50801t4	-9.6	34.5 + 0.4 - 0.4	13.1 + 0.8 - 0.8	a > 1.82, e > .10, 10.9 < i < 21.5
u2om1201t4	5.0	98.7 + 2.6 - 2.0	70.2 + 1.4 - 1.1	a > 2.32, e > .21, 07.5 < i < 19.5
u2ot0q01t4	2.7	24.6 + 0.2 - 0.4	-7.2 + 0.1 - 0.1	a > 2.18, e > .21, 04.6 < i < 14.2
u2ov2j01t3	-0.3	39.9 + 0.9 - 1.0	7.0 + 0.9 - 1.0	a > 1.88, e > .07, 03.2 < i < 13.9
u2ov5601t2	0.7	40.9 + 2.0 - 1.9	-8.9 + 0.7 - 0.7	a > 1.25, e > .23, 03.1 < i < 90.1
u2ov5d01t3	0.7	21.7 + 0.4 - 0.6	-7.0 + 0.04 - 0.1	a > 2.32, e > .21, 07.8 < i < 19.7
u2ov6f01t4	3.9	36.9 + 6.0 - 0.2	14.6 + 3.3 - 0.1	a > 2.48, e > .01, 03.9 < i < 06.9
u2ov7t01t4	-5.0	41.3 + 1.5 - 1.1	-11.4 + 0.1 - 0.1	a > 2.24, e > .07, 05.5 < i < 12.2
u2ov9w01t2	-3.7	43.6 + 3.3 - 3.6	-27.3 + 1.1 - 1.2	a > 2.57, e > .05, 09.6 < i < 13.0
u2ova001t4	-3.6	52.9 + 0.9 - 1.4	3.6 + 0.8 - 1.2	a > 1.78, e > .07, 04.5 < i < 18.4
u2ovab01t2	-10.6	26.6 + 0.3 - 0.2	-5.8 + 0.3 - 0.2	a > 2.33, e > .11, 18.0 < i < 40.8
u2sw0501t1	-1.7	47.5 + 1.7 - 1.8	13.5 + 0.4 - 0.4	a > 2.25, e > .13, 03.9 < i < 04.1
u2w90701t1	4.1	32.5 + 6.4 - 6.1	-19.4 + 2.0 - 1.9	a > 2.70, e > .07, 06.3 < i < 13.2
u33l3801m3	4.0	113.6 + 9.8 - 9.2	-135.3 + 3.1 - 2.9	a > 1.98, e > .19, 25.9 < i < 52.1
u3800201t1	7.2	38.6 + 3.9 - 3.9	18.3 + 1.1 - 1.1	a > 2.78, e > .05, 07.8 < i < 14.8



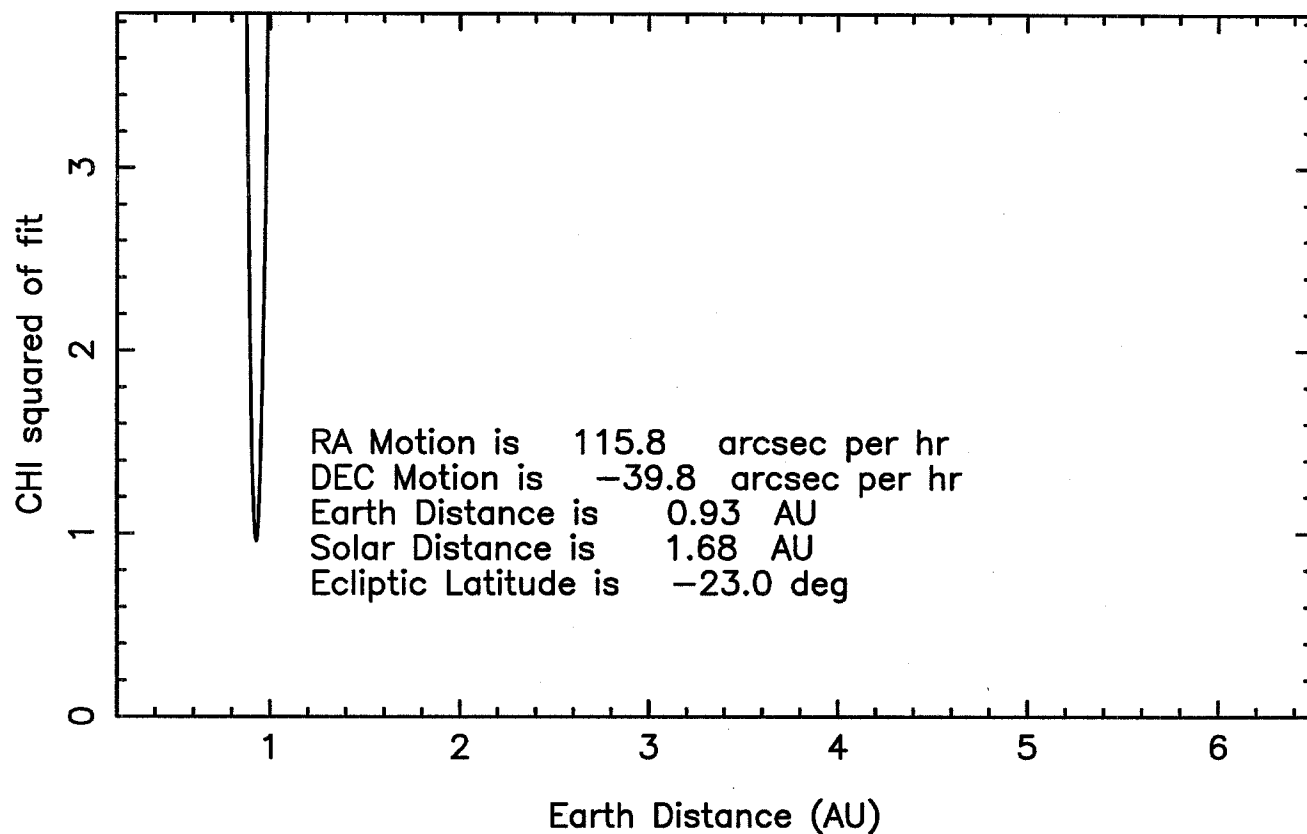




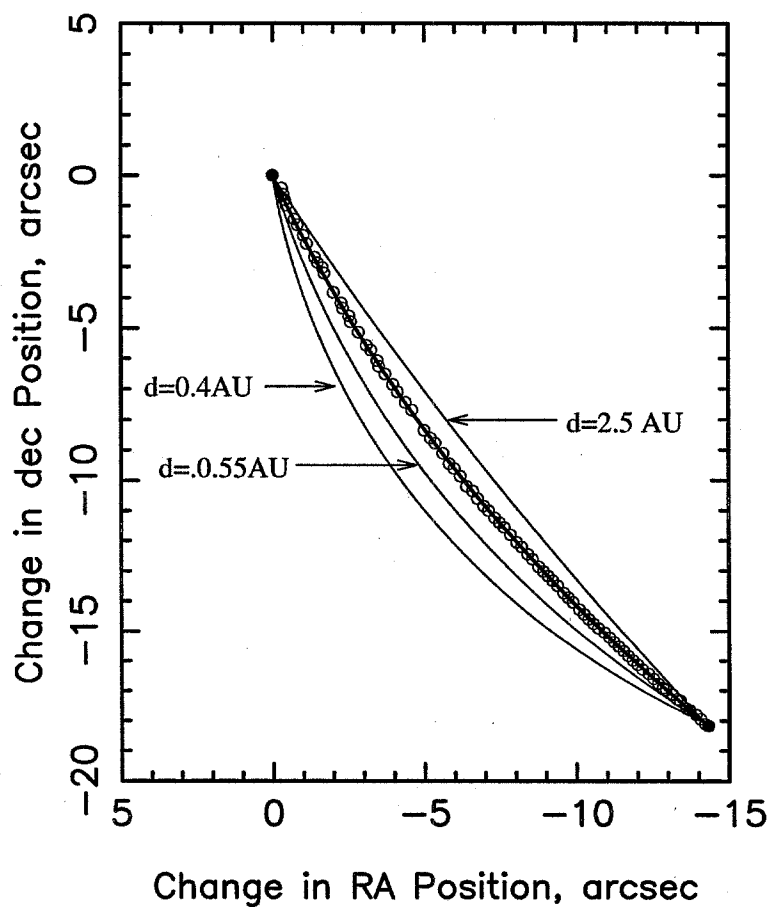


f5

Solution for images u2805m01t4-u2805m01t4

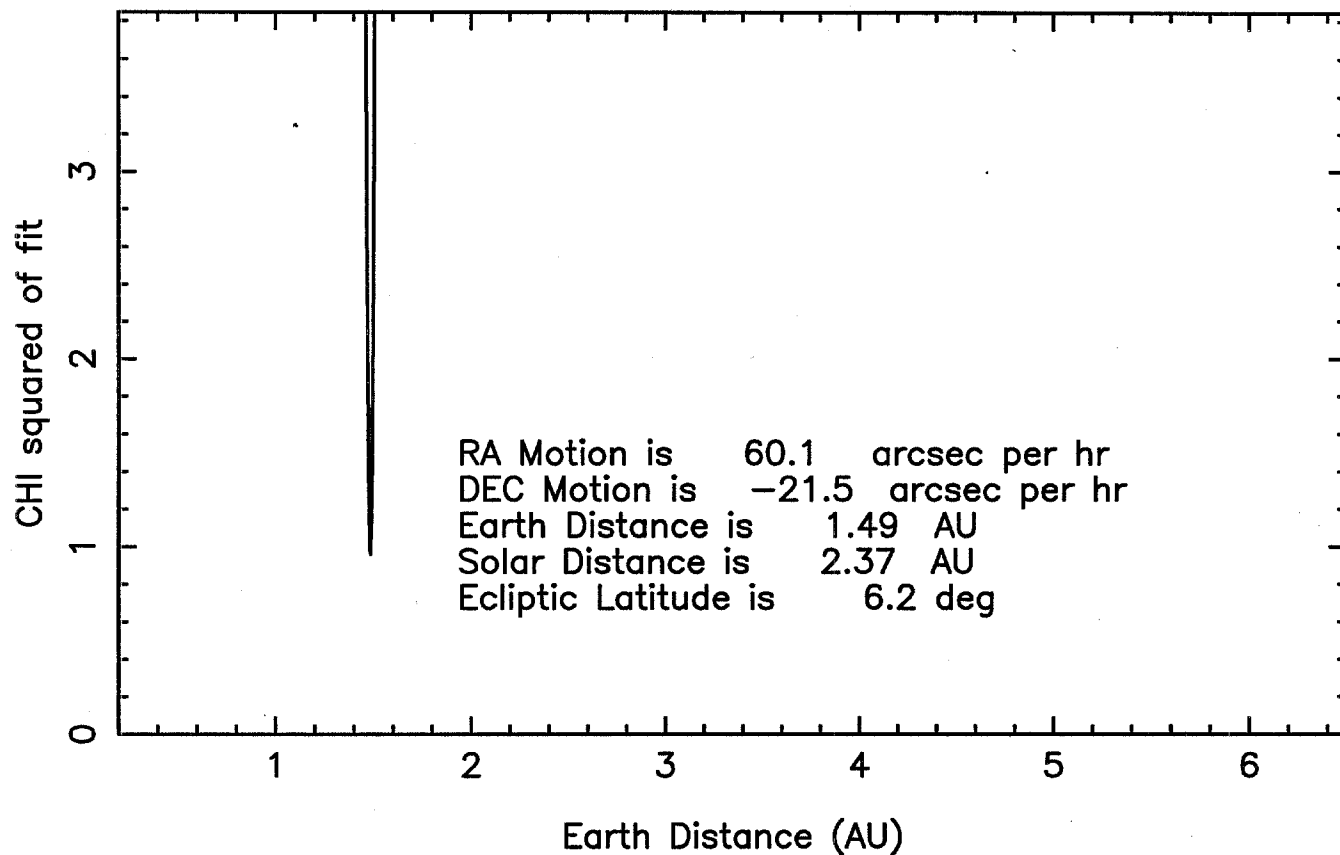


Data/model comparison for images u2805m01t4 u2805m01t4

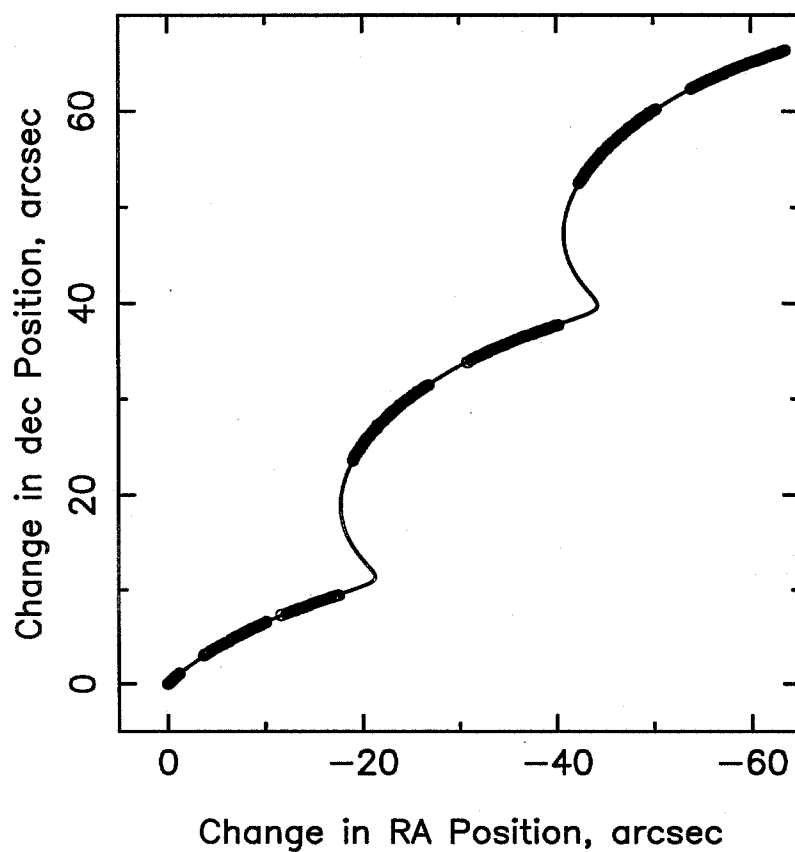


fl

Solution for images u2b40401t3–u2b40405t1

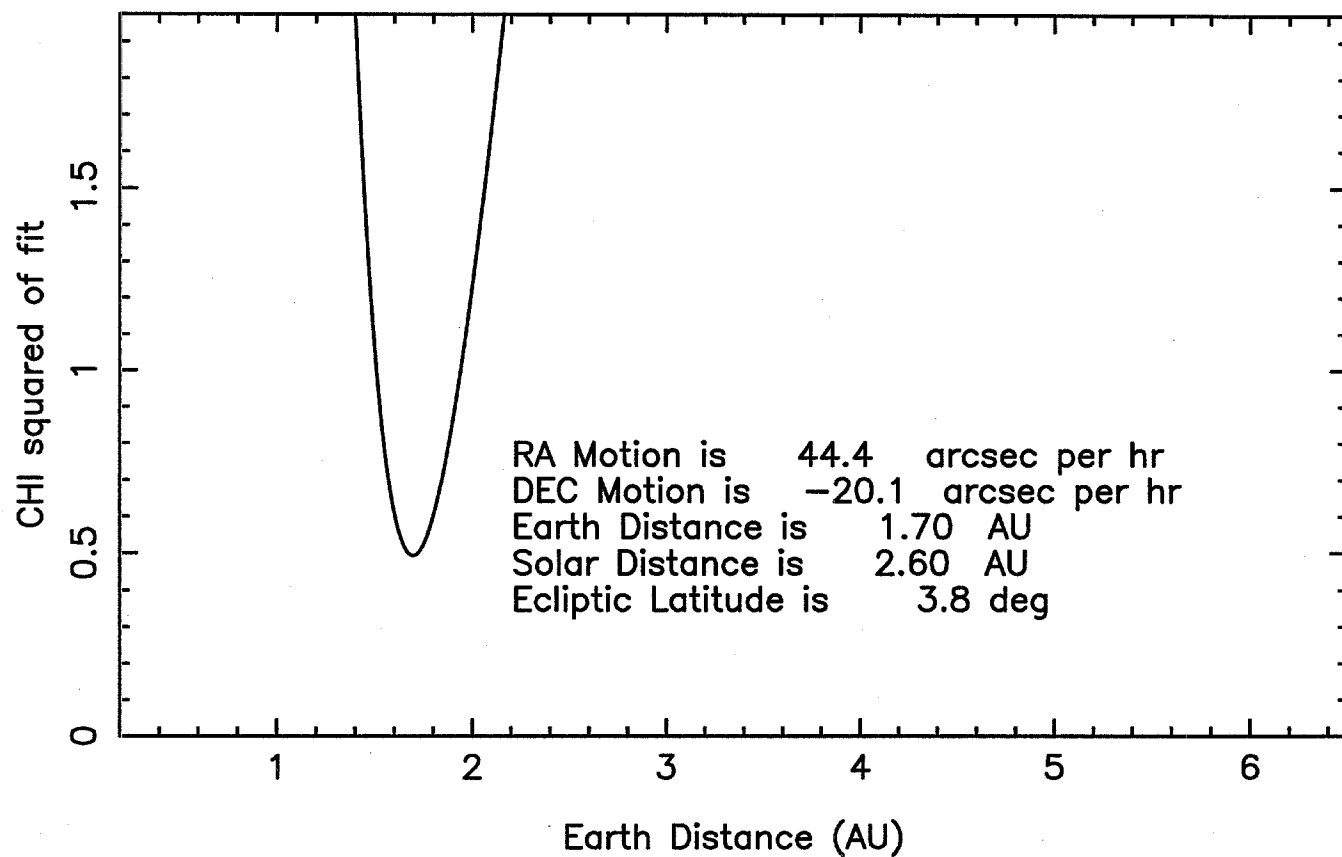


Data/model comparison for images u2b40401t3 u2b40405t1

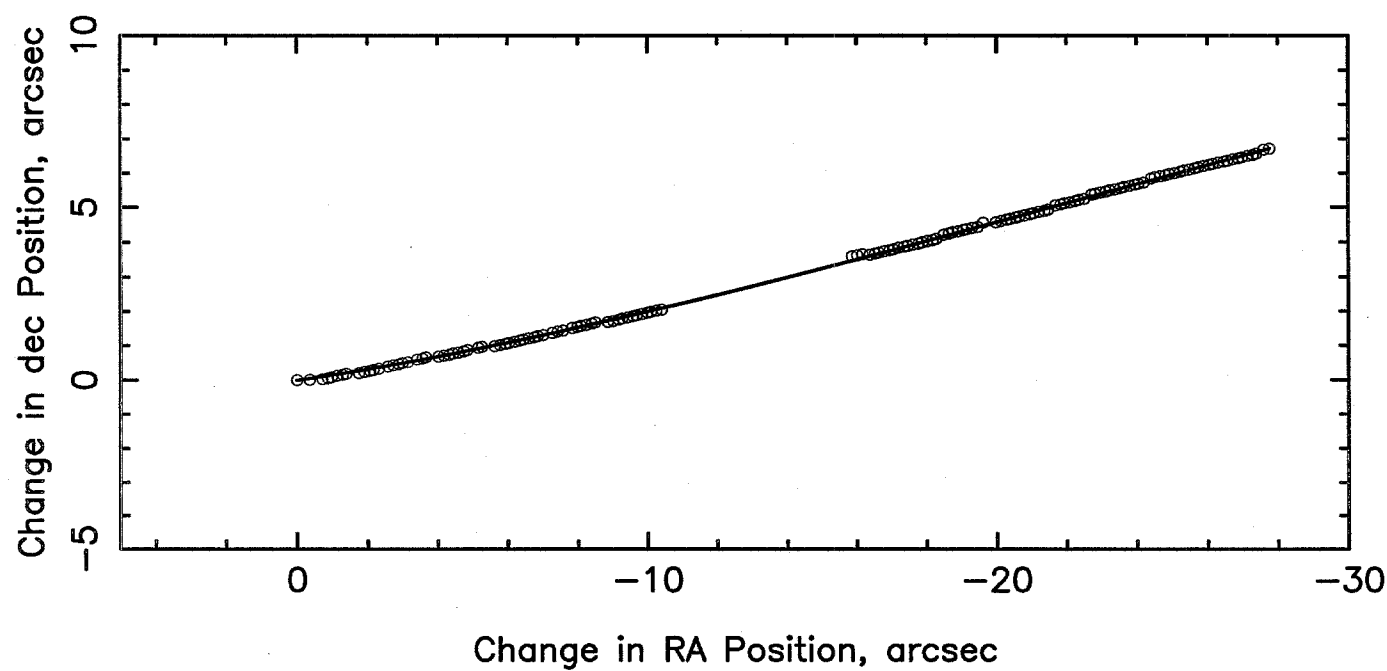


f7

Solution for images u26g0e02t4–u26g0e03t4

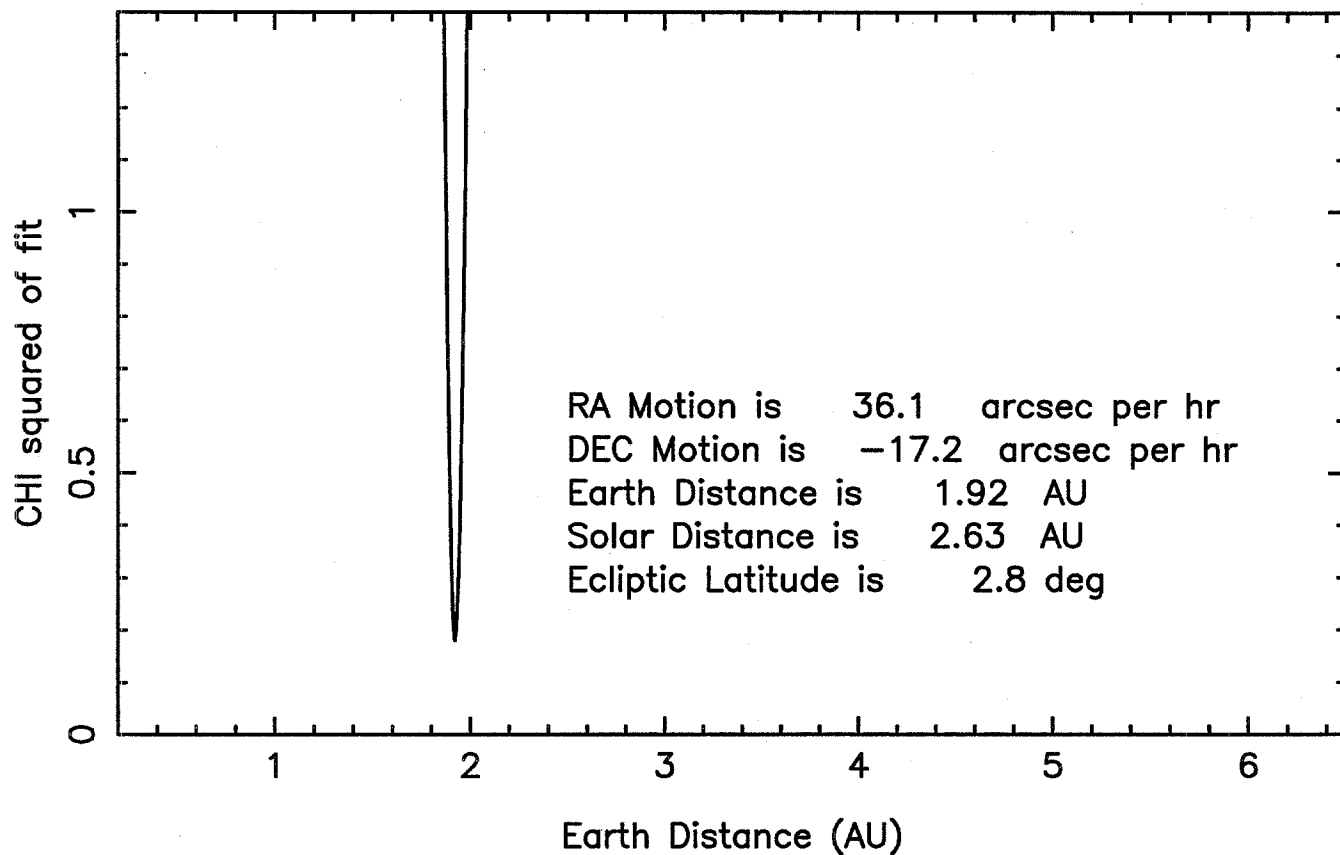


Data/model comparison for images u26g0e02t4 u26g0e03t4

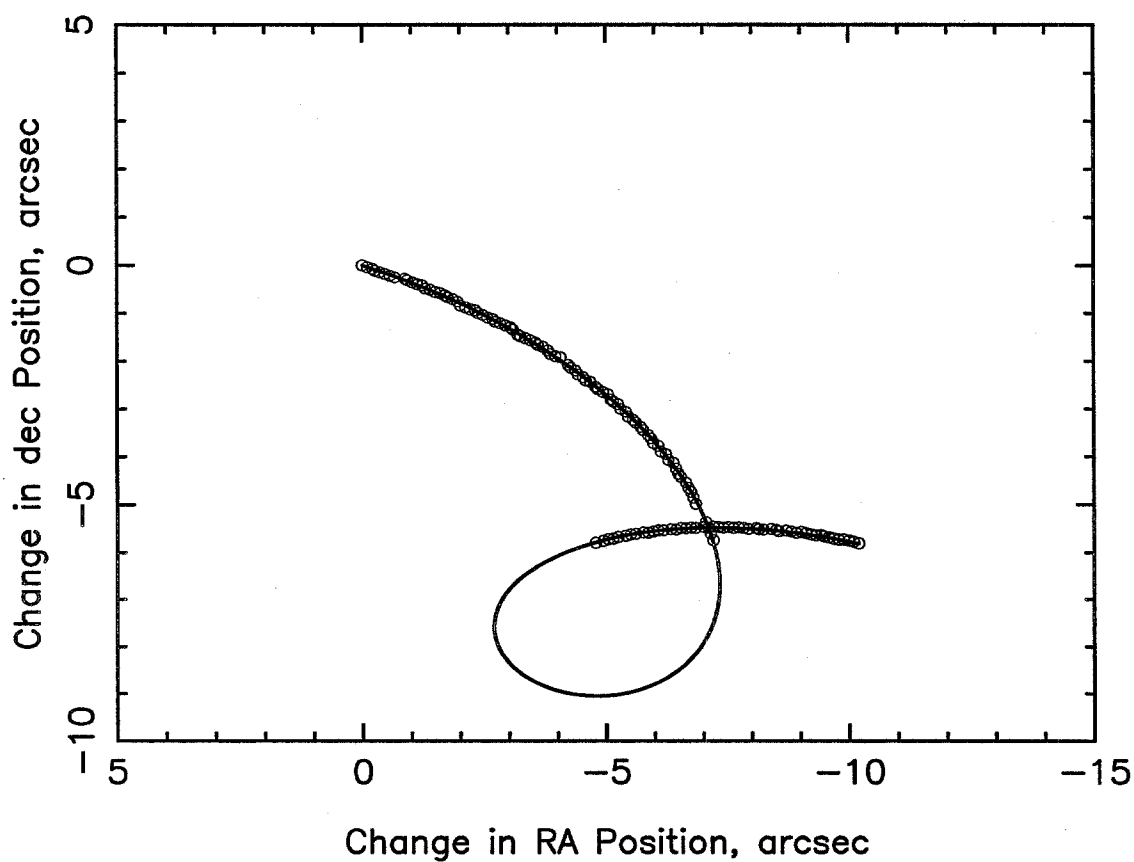


f8

Solution for images u26g0601t4–u26g0602t4

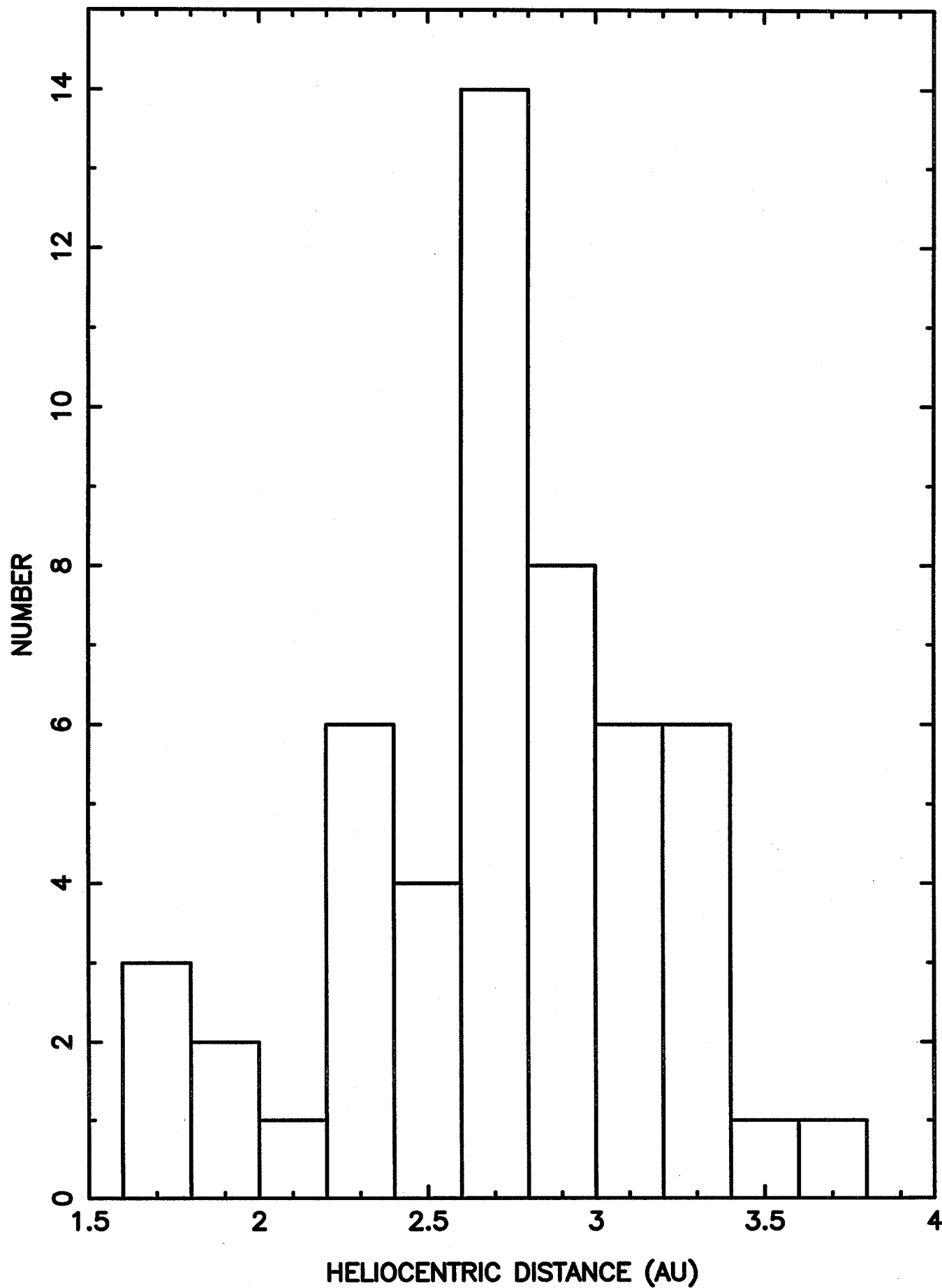


Data/model comparison for images u26g0601t4 u26g0602t4

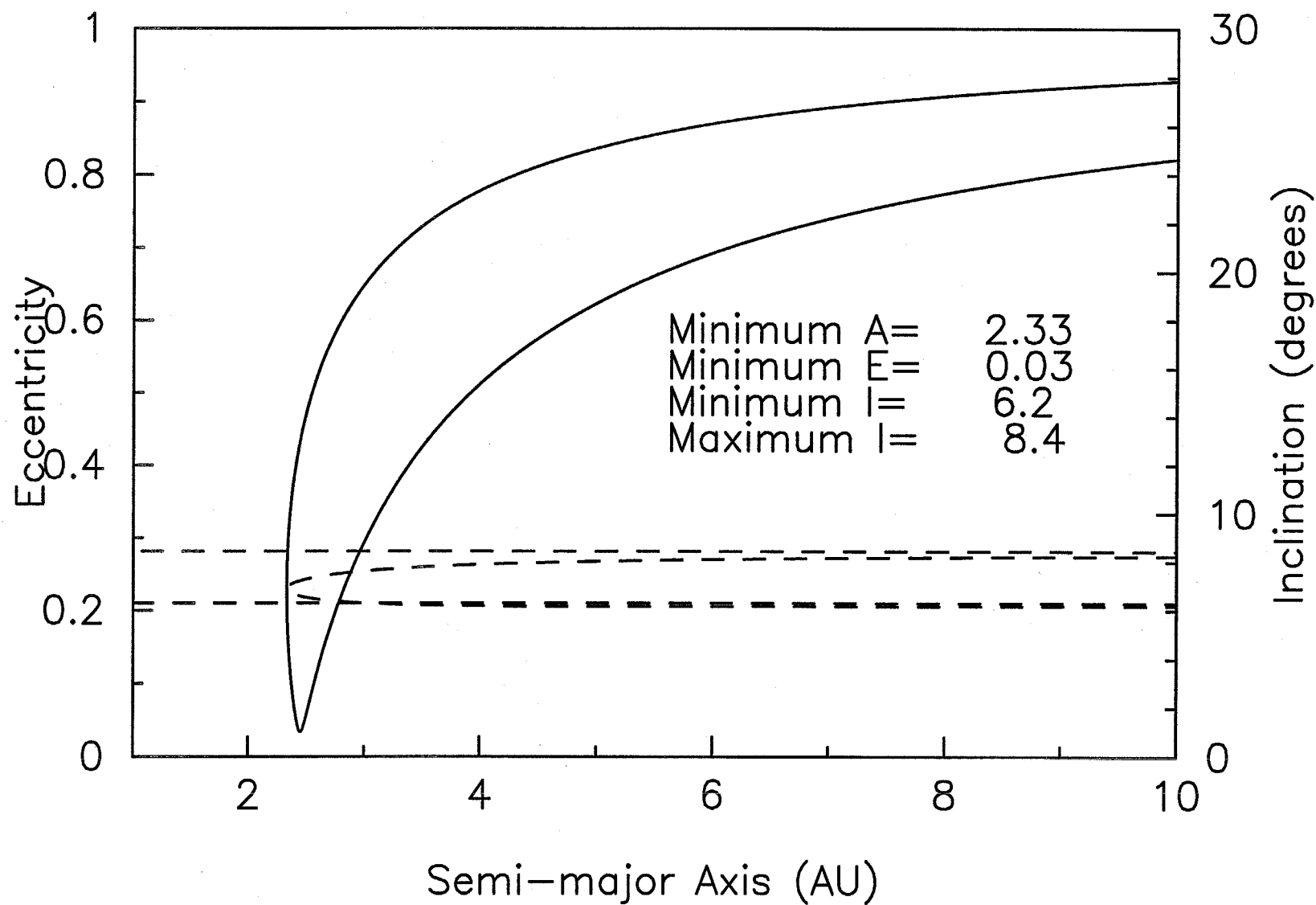


49

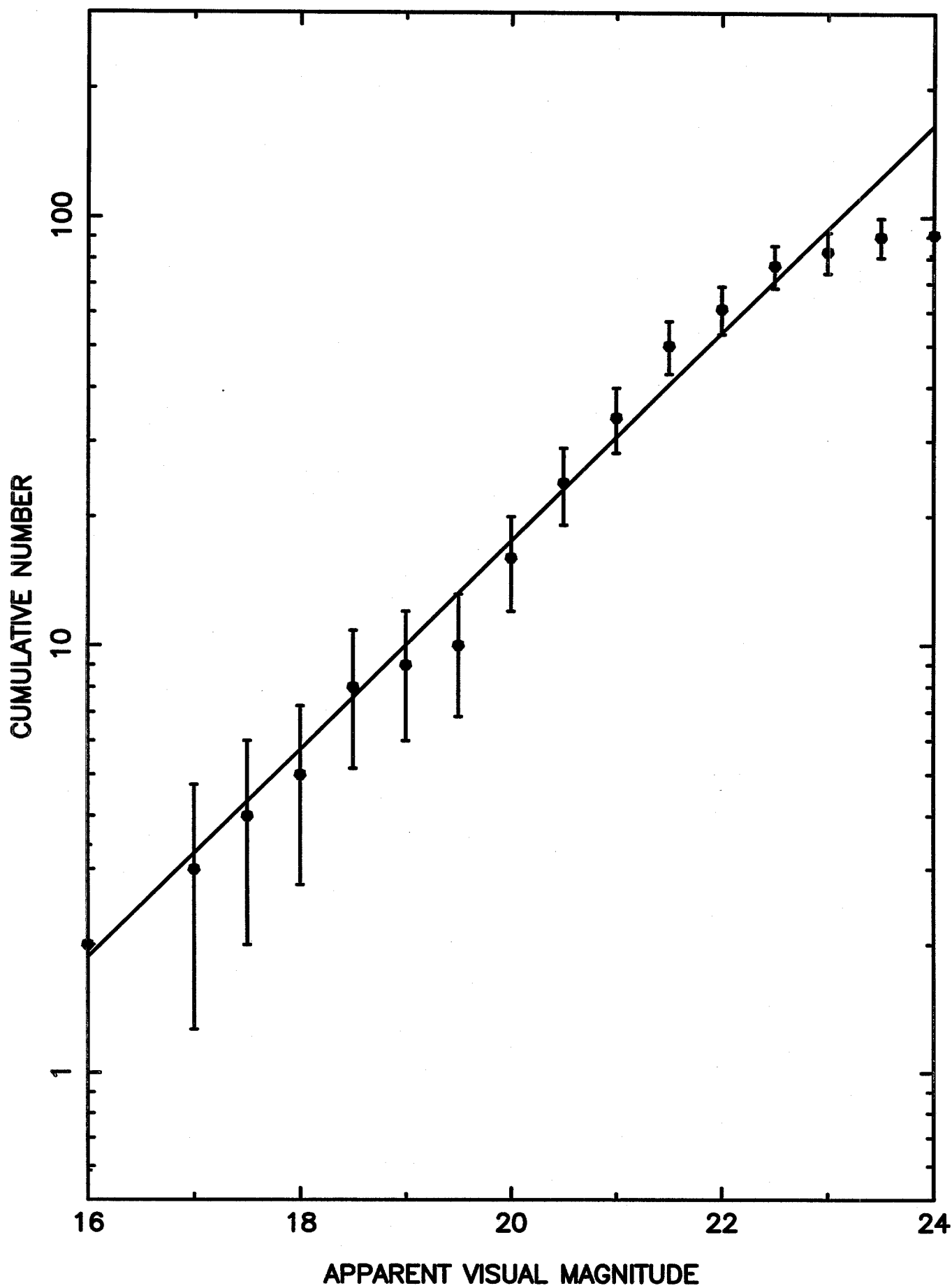
HELIOCENTRIC DISTANCE OF HST ASTEROIDS



Orbit constraints for images u2b40401t3-u2b40405t1

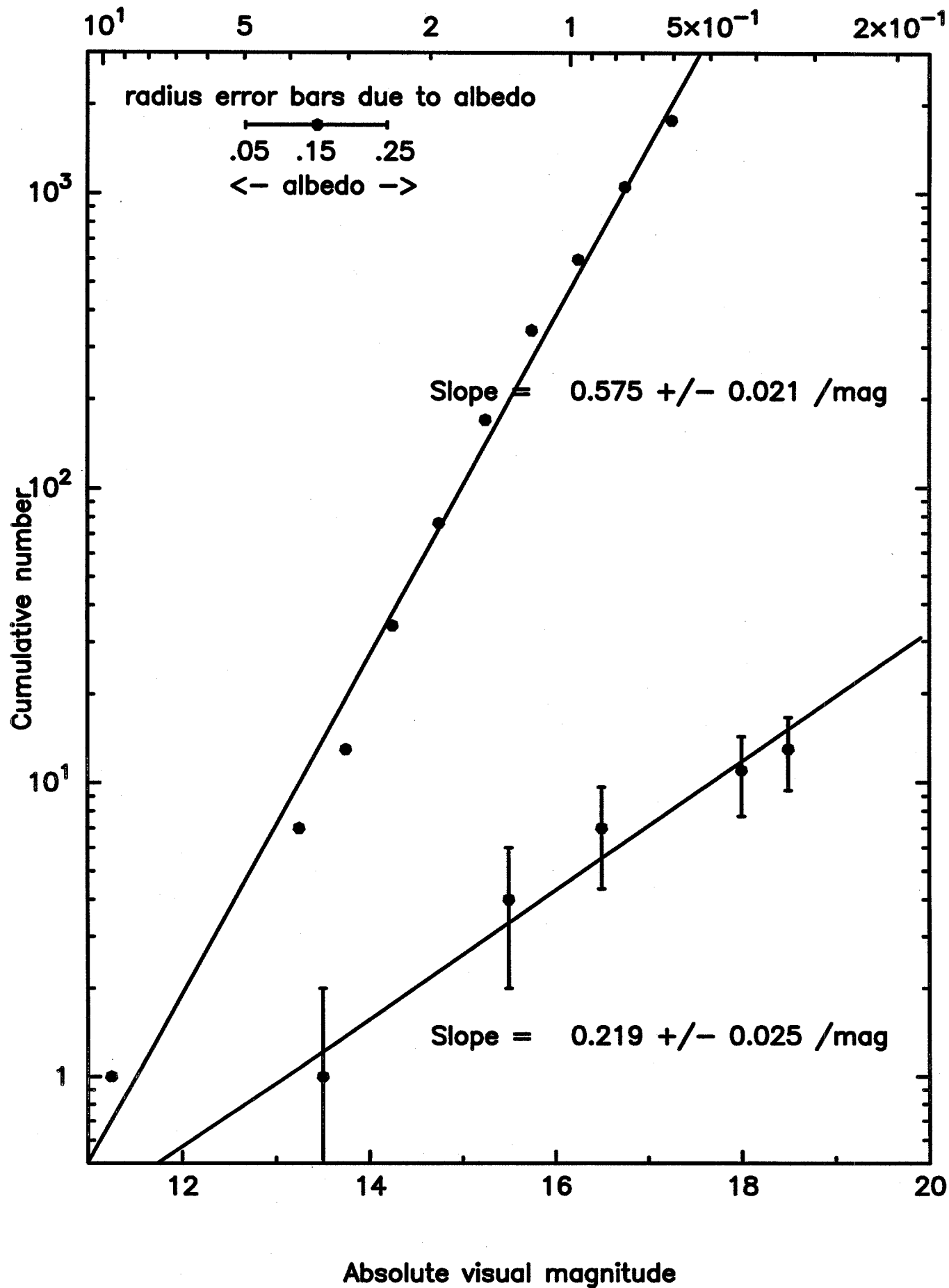


HST ASTEROID MAGNITUDES



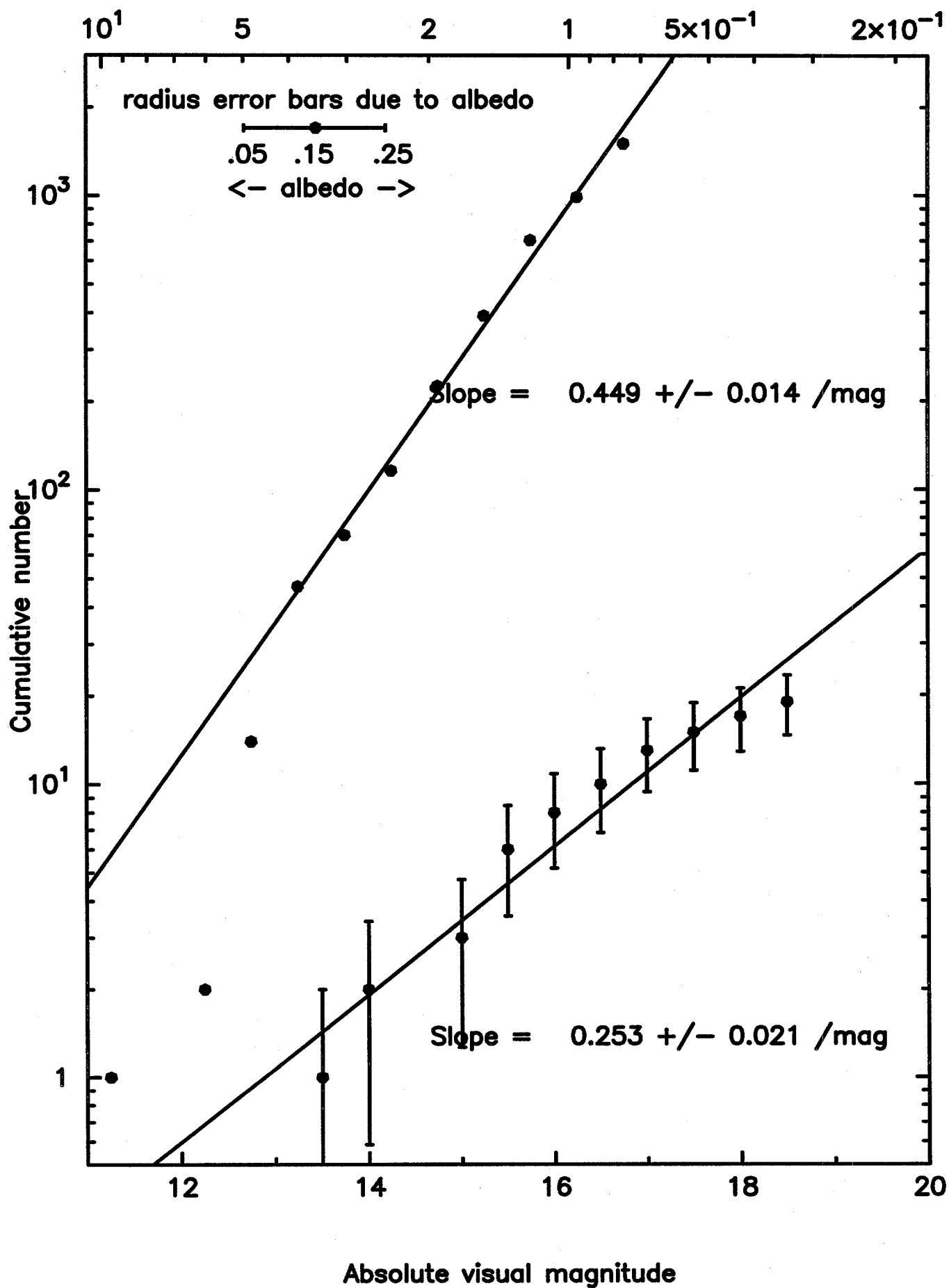
f12a

Log asteroid radius (km) $2 < a < 2.6$ AU



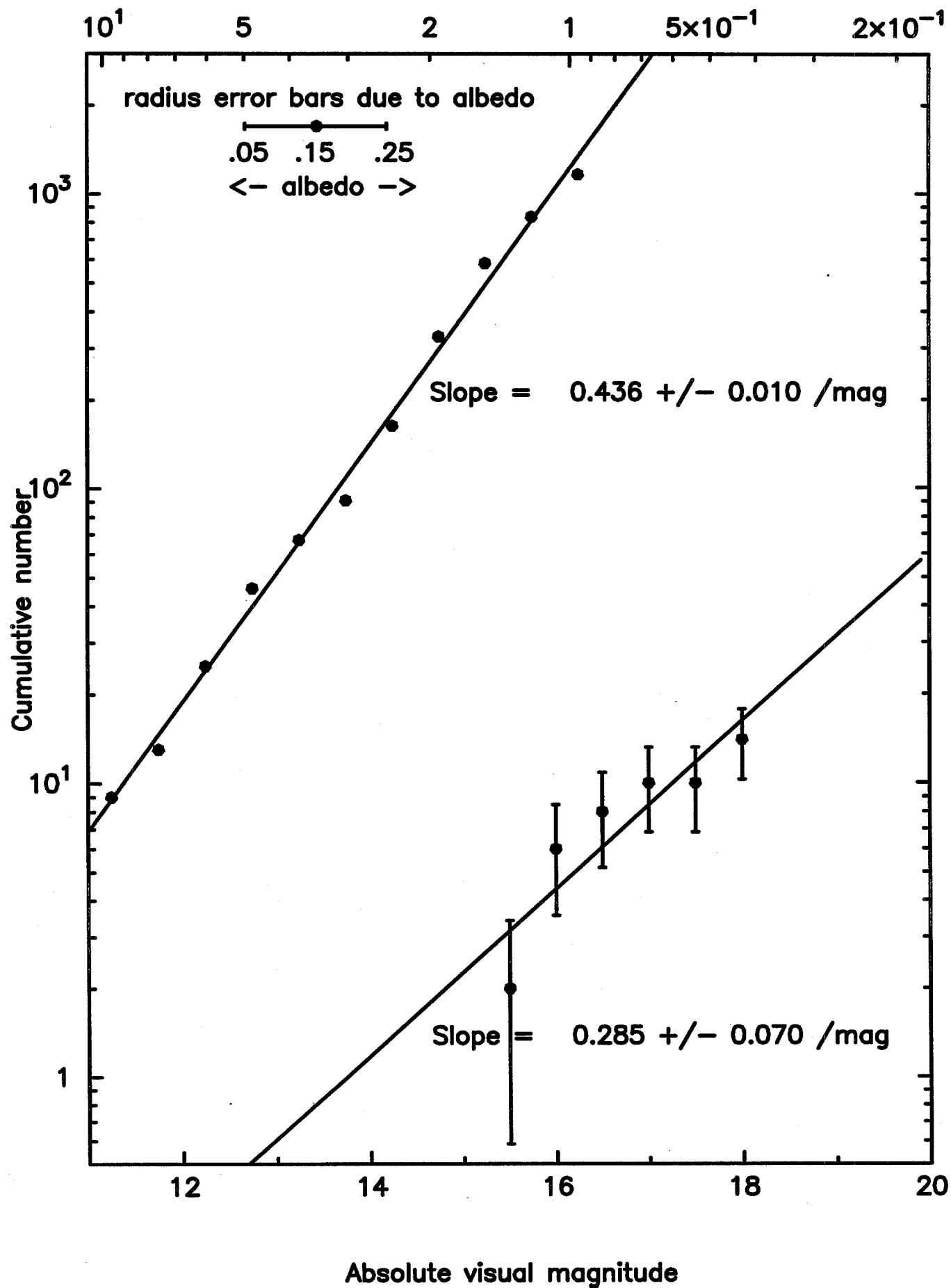
f126

Log asteroid radius (km) $2.6 < a < 3$ AU



f12c

Log asteroid radius (km) $3 < a < 3.5$ AU



HELIOCENTRIC LATITUDE OF HST ASTEROIDS

